Plasma Sources Science and
Technology

TOPICAL REVIEW • OPEN ACCESS

Kinetic electron cooling in magnetic nozzles: experiments and modeling

To cite this article: June Young Kim *et al* 2023 *Plasma Sources Sci. Technol.* **32** 073001

OPEN ACCESS
IOP Publishing

Plasma Sources Science and Technology

Plasma Sources Sci. Technol. **32** (2023) 073001 (27pp)

https://doi.org/10.1088/1361-6595/acd71c

Topical Review

Kinetic electron cooling in magnetic nozzles: experiments and modeling

June Young Kim[1,*], Kyoung-Jae Chung[1], Kazunori Takahashi[2], Mario Merino[3] and Eduardo Ahedo[3]

[1] Department of Nuclear Engineering, Seoul National University, Seoul, Republic of Korea
[2] Department of Electrical Engineering, Tohoku University, Sendai, Japan
[3] Equipo de Propulsión Espacial y Plasmas (EP2), Universidad Carlos III de Madrid, Madrid, Spain

E-mail: beacoolguy@snu.ac.kr

Received 14 December 2022, revised 24 April 2023
Accepted for publication 19 May 2023
Published 14 July 2023

CrossMark

Abstract

As long-distance space travel requires propulsion systems with greater operational flexibility and lifetimes, there is a growing interest in electrodeless plasma thrusters that offer the opportunity for improved scalability, larger throttleability, running on different propellants and limited device erosion. The majority of electrodeless designs rely on a magnetic nozzle (MN) for the acceleration of the plasma, which has the advantage of utilizing the expanding electrons to neutralize the ion beam without the additional installation of a cathode. The plasma expansion in the MN is nearly collisionless, and a fluid description of electrons requires a non-trivial closure relation. Kinetic electron effects and in particular electron cooling play a crucial role in various physical phenomena, such as energy balance, ion acceleration, and particle detachment. Based on experimental and theoretical studies conducted in recognition of this importance, the fundamental physics of the electron-cooling mechanism revealed in MNs and magnetically expanding plasmas is reviewed. In particular, recent approaches from the kinetic point of view are discussed, and our perspective on the future challenges of electron cooling and the relevant physical subject of MN is presented.

Keywords: electric propulsion, magnetic nozzle, electron thermodynamics, electron cooling, adiabatic process, electron kinetics, ExB source

(Some figures may appear in colour only in the online journal)

1. Introduction

In the development of technology for deep-space exploration of long-duration space missions, space propulsion requires higher thrust efficiency and a longer lifetime. Magnetic nozzle (MN)-based devices are attracting attention as next-generation electric thrusters, with advantages such as contactless and electrodeless plasma acceleration, enabling a higher throttleablity range, and facilitating the use of alternative propellants (Arefiev and Breizman 2005, Ahedo 2011a, Sutton 2016, Merino and Ahedo 2017, Levchenko *et al* 2020, Sheppard and Little 2020, Takahashi 2020b). Three-dimensional steerable MNs have also been proposed and demonstrated for the simplified adjustment of ion-beam trajectory and thrust vector control (Charles *et al* 2008, Merino

[*] Author to whom any correspondence should be addressed.

and Ahedo 2016a, Merino and Ahedo 2018, Imai and Takahashi 2021, Takahashi and Imai 2022). The MN has been recognized as the acceleration stage in the development of next-generation space plasma thrusters, such as the applied-field magneto plasma dynamic thruster (AF-MPDT) (Choueiri 1998, Kodys and Choueiri 2005, Andrenucci 2010), the helicon plasma thruster (HPT), (Ziemba *et al* 2005, Takahashi *et al* 2011b, Takahashi 2019), the electron cyclotron resonance plasma thruster (ECRT) (Sercel 1987, Vialis *et al* 2018, Correyero *et al* 2019), and variable specific impulse plasma rocket (VASIMIR) (Chang-Diaz 2000a, 2000b, Arefiev and Breizman 2004) using alternative currents ranging from radiofrequency (RF) to microwave (MW) power sources. The proposed electric thrusters have different characteristics from the plasma generation and heating viewpoint, but the physics of the quasineutral, quasi-collisionless plasma expansion in the MN are essentially common for all of them: the diverging magnetic field confines the plasma radially and helps convert perpendicular energy into parallel energy, while the thermal energy available in the electrons is converted to ion kinetic energy via the self-consistent electrostatic field. The electron response, in particular their temperature, plays a fundamental role in the setup of the electrostatic field in the plume, which is responsible for ion acceleration (Hooper 1993, Breizman *et al* 2008, Deline *et al* 2009, Ahedo and Merino 2011, 2012, Ebersohn *et al* 2012, Little and Choueiri 2013, Merino and Ahedo 2014, Olsen *et al* 2015, Takahashi and Ando 2017b, Little and Choueiri 2019). Accordingly, for the development of MN-based devices, it is essential to understand the kinetics of electron cooling along the divergent magnetic field.

A collisionless, magnetically expanding plasma has quite complex physical elements, and overlooking the kinetics of electrons (e.g. by using a single fluid approach with either isothermal or polytropic closures) can dictate the wrong directions in device development (Kaganovich *et al* 2020). Crucially, the global electron kinetic response in the MN determines electron thermodynamics. The plasma expansion in MN-based devices is driven by the thermal energy in the plasma, and with a few exceptions, most of the thermal energy is in the electron species. The electron temperature map T_e, in particular, determines the electrostatic potential map ϕ in the plume, which in turn defines the ion energy far downstream. The electron temperature T_e also determines the strength of the azimuthal electron currents, responsible for the generation of magnetic thrust and the plasma-induced magnetic field. Hence, the correct understanding of electron kinetics and electron cooling in the MN is essential for the analysis of the operation of these devices and their optimization.

The invariants of particle motion in electric and magnetic fields (the conservation of energy and magnetic moment) result in a complex electron velocity distribution function (EVDF) in the MNs, e.g., an anisotropic and partially depleted EVDF (Martinez-Sanchez *et al* 2015, Merino *et al* 2018, Sanchez-Arriaga *et al* 2018, Ahedo *et al* 2020, Merino *et al* 2021). Electrons are classified into free, reflected, and doubly-trapped populations according to the effective potential that defines their motion (Martinez-Sanchez *et al* 2015). The doubly-trapped electron population, whose trajectories are disconnected from the plasma source, depends on the transient plume setup process and the weak collisionality that may exist in the plasma. In accordance with this complexity, recent modeling results provide clues on the interpretation of the thermodynamic state of electrons far from local equilibrium, emphasizing that the heat flux of anisotropic energy has a dominant role in the electron energy equation (Merino *et al* 2018, Ahedo *et al* 2020, Hu *et al* 2021, Merino *et al* 2021).

Measurements of the EVDF have revealed the kinetic behavior of the electrons in the MN. The EVDF measured in the source has shown a depleted tail at the break energy corresponding to the potential drop, i.e., the EVDF has a high-temperature, low-energy population and a low-temperature, high-energy population. The former is trapped by the electric field, while the latter can overcome the electric field and neutralize the supersonic ion beam (Plihon *et al* 2007, Takahashi *et al* 2011a, Takahashi and Ando 2017a). Since the energization of the electrons is due to the RF heating near the antenna, the spatial mapping of the EVDFs has also clarified some kinetic aspects of the electron transport dynamics and structural formation (Takahashi *et al* 2009, Charles 2010, Takahashi *et al* 2017a, Gulbrandsen and Fredriksen 2017, Ghosh *et al* 2017). Recent experimental studies have tried to determine the thermodynamic state of electrons in electric and magnetic fields (Sheehan *et al* 2014, Lafleur *et al* 2015, Little and Choueiri 2016, Zhang *et al* 2016a, Kim *et al* 2018, Takahashi *et al* 2018, Kim *et al* 2019, 2021a, 2021b, Takahashi *et al* 2020a, Boni *et al* 2022, Vinci *et al* 2022). Although more effort is required to experimentally prove the anisotropic behavior of electrons predicted by the theoretical works, the analysis of the spatial distribution of electron properties gives rise to a major contribution to the establishment and verification of the theory for the electron cooling process. Recent studies (Kim *et al* 2018, Takahashi *et al* 2018, Kim *et al* 2019, Takahashi *et al* 2020a, Kim *et al* 2021a, 2021b) have succeeded in finding out that each electron group can have a different thermodynamic state based on the classification of electrons suggested by the models, and this advancement in knowledge has presented a new perspective on the anomalous quasi-isothermal behavior of electrons in the divergent magnetic field observed in the universe and laboratory plasmas, as well as improving the performance of MN devices. In the development of electrodeless propulsion, the consensus found between theoretical and experimental studies demands a summary of the essential topic of electron cooling that has been explored for about 50 years (Andersen *et al* 1969, Kuriki and Okada 1970, Litvinov 1971, Raadu 1979, Arefiev and Breizman 2008). We believe that this work will be a stepping stone in the expansion of the research field to various topics scattered for improving the performance of MNs and for physical understanding. Additionally, this study is expected to provide valuable insights into characterizing and developing plasma sources for various applications, including plasma processes (Conrads and Schmidt 2000) and accelerators (Agnihotri *et al* 2011) that employ expanding magnetic field structures. We note that the body of research on plasma expansions in applications other than space propulsion is vast and also relevant (Denavit 1979, Samir *et al* 1983, Boyd and Ketsdever 2001, Mora 2003, Capitelli *et al* 2004, Drake and Drake 2006, Gopal *et al* 2013, Versolato 2019). Plasma expansions in the context of plasma thrusters are characterized by low electron temperatures (1–5 eV), low-to-mild plasma densities ($10^{13}-10^{16}\,\mathrm{m}^{-3}$), hypersonic ion Mach numbers (5–20), and being globally current-free. In the case of MNs, the plasma expansion results in well-magnetized electrons, while ions can have any degree of magnetization depending on the device. In this regard, we provide a review of the kinetic features of electron cooling in an MN.

The rest of the paper is structured as follows. Section 2 presents and discusses relevant experimental results to understand electron cooling and kinetic effects in a MN. Section 3 summarizes the basic fluid model of the plasma expansion in a MN, and then examines electron cooling from a theoretical viewpoint, reviewing recent modeling and numerical results. Finally, Section 4 gathers the main conclusions and outlines the open challenges in this matter.

2. Experimental approach to electron thermodynamics in MNs

Experimental environments to elucidate the thermodynamic state of electrons in the MN require low collisionality, minimized plasma-solid boundary effects, and closed paths of magnetic field lines. Based on these requirements, the experimental study of electron thermodynamics is to magnetically expand plasma generated in the source region into a diffusion region having a larger volumetric dimension than the source and to analyze the behavior of the plasma using a (local) polytropic exponent. In recent years, intensive studies on the subject of electron thermodynamics have been carried out in the laboratory (tables 1 and 2). They have engineering and physical significance in that they present a new perspective on the thermodynamic state of electrons relevant to not only the operating mechanism of MNs but also the fundamental physics of space plasmas (Sheehan *et al* 2014, Lafleur *et al* 2015, Little and Choueiri 2016, Zhang *et al* 2016a and 2016b, Kim *et al* 2018, Takahashi *et al* 2018, Kim *et al* 2019, Takahashi *et al* 2020a, Kim *et al* 2021a, 2021b, Boni *et al* 2022, Vinci *et al* 2022).

On the basis of the diagnostics technique and plasma source technology, the electron cooling rate was investigated in relation to a simple description of the ion acceleration in the MN (Sheehan *et al* 2014, Lafleur *et al* 2015, Zhang *et al* 2016a). Then recent comprehensive experiments have taken into account detailed elements, such as the trapped motion, the cross-field diffusion, and the degree of freedom of electrons (Kim *et al* 2018, Takahashi *et al* 2018, Kim *et al* 2019, Takahashi *et al* 2020a, Kim *et al* 2021a, 2021b). Accordingly, this section emphasizes the sequential flow of experimental research and classifies studies into (1) initial studies that do not consider all the factors (the trapped motion, the cross-field diffusion, and degree of freedom), (2) studies that consider the effect of trapped electrons on thermodynamics, and (3) studies that control the thermodynamic state of electrons by modifying the number of degrees of freedom.

2.1. Basic research on electron thermodynamics

Early studies excluded the in-depth discussion of the thermodynamics of electrons, but rather introduced a polytropic index to provide a simple description of electron cooling in MN devices (Sheehan *et al* 2014). The experimental study of electron thermodynamics in MNs was revisited during the development of VASIMR. The experiments in the high-vacuum chamber of Ad Astra Company (4.23 m in diameter and 10 m long with a base pressure of 10^{-9} Torr) minimized the blocking of the streamline of the magnetic field by the vacuum wall, and thus an experiment in more realistic boundary condition similar to space environment was performed with the helicon source-based MN (VX-200), a prototype electrodeless plasma propulsion device for spacecraft [figure 1]. The main objective of the study was to elucidate the physical meaning of the electron cooling rate, the correlation of the plasma potential and electron temperature and density varying along the divergent magnetic field. In the same context, an essential question is presented: can a current-free double layer observed in some laboratory experiments be created in a space-like environment?

Sheehan *et al* (2014) proposed the correlation of the electron cooling and ambipolar ion acceleration in a MN. They concluded that the plasma system of the MN is adiabatic (i.e., it does not exchange energy with its surroundings) in the expansion region, so any energy lost by the electrons must be transferred to the ions via the electric field.

They classified three possible theories of electron cooling and relevant ambipolar acceleration mechanisms based on previous studies: (1) current-free double layer: a potential gradient equivalent to 10 s of electron temperature is generated within a few Debye lengths from the plasma source, and electrons and ion energetic beams are created on the high and low potential side of the double layer, respectively; (2) rarefaction wave theory: a rarefaction wave creates a large potential barrier in the far-downstream region, and electrons lose their energy and become trapped downstream with decreased energy; and (3) adiabatic theory combined with electron momentum equation: generation of an electric field that induces ion acceleration due to the electron cooling (adiabatic) process.

Experimental evidence corresponding to the double layer and rarefaction wave theory (such as a strong electric potential layer in a region of tens of Debye lengths near the nozzle throat or in the far-field region) was not observed. Rather, only the relation between the electron temperature T_e and the plasma potential $e\phi$ enables a discussion of the electron thermodynamics by the relation, $\partial(e\phi)/\partial s=\gamma/(\gamma-1)\,\partial T_e/\partial s$, where s is the field-aligned pointing vector and γ is the polytropic index of electrons [figure 2]. They considered that T_e measured with the planar probe only collects the temperature component parallel to the magnetic field, $T_{e,\|}$. Accordingly, γ becomes about 1.75 by multiplying 2 by the coefficient of the relation $\partial(e\phi)/\partial s=1.17\partial T_{e,\|}/\partial s$ obtained from the experimental values. Considering that the estimated γ exceeds 5/3 in the relation between the electron density and $e\phi$, it was concluded that the instability may play a crucial role in the plasma

Table 1. Details of experimental information for representative studies of the electron thermodynamics in magnetic nozzles.

References	Neutral pressure	Source type	Magnetic field	Vacuum chamber or expansion chamber
Sheehan *et al* (2014)	0.1 mTorr	Helicon (6.78 MHz)	Electromagnet (2000 G at nozzle throat)	Vacuum chamber (4.2 m in diameter and 10 m in length)
Lafleur *et al* (2015)	3.8–7.5 μTorr	ECR (2.45 GHz)	Electromagnet (<1000 G inside the source)	Vacuum chamber (1 m in diameter, 4 m in length)
Little and Choueiri (2016)	0.02 mTorr	ICP (13.56 MHz)	Electromagnet (peak magnetic field, 150–420 G)	Vacuum chamber (2.4 m in diameter, 7.6 m in length)
Zhang *et al* (2016a)	0.3 mTorr	Helicon (13.56 MHz)	Electromagnet (peak magnetic field, 150 G)	Expansion chamber (0.32 m in diameter, 0.3 m in length)
Takahashi *et al* (2018)	0.5 mTorr	DC	Electromagnet (peak magnetic field, 220 G)	Expansion chamber (0.15 m in diameter, 0.5 m in length)
Kim *et al* (2018)	0.45 mTorr	ECR (2.45 GHz)	Electromagnet (450 G at nozzle throat)	Expansion chamber (0.6 m in diameter, 0.66 m in length)
Kim *et al* (2019)	0.4 mTorr	ICP (13.56 MHz)	Electromagnet (70 G at nozzle throat)	Expansion chamber (0.6 m in diameter, 0.66 m in length)
Correyero *et al* (2019)	2.1–2.8 μTorr	ECR (2.45 GHz)	Electromagnet or permanent magnet (fixed at 900 G for both types at the thrust back plate)	Vacuum chamber (0.8 m in diameter, 2 m in length)
Takahashi *et al* (2019)	0.5 mTorr	DC	Electromagnet (peak magnetic field, 264 G)	Expansion chamber (0.15 m in diameter, 0.5 m in length)
Kim *et al* (2021a)	0.4 mTorr	DC	Electromagnet (230 G at nozzle throat)	Expansion chamber (0.6 m in diameter, 0.66 m in length)
Kim *et al* (2021b)	0.4 mTorr	DC	Electromagnet (230 G at nozzle throat)	Expansion chamber (0.6 m in diameter, 0.66 m in length)
Vinci *et al* (2022)	0.7 mTorr	Helicon (13.56 MHz)	Electromagnet (peak magnetic field, 86 $\pm$ 3 G)	Expansion chamber (0.3 m in diameter, 0.5 m in length)

Table 2. Details of diagnostics and the measured polytropic index.

References	Probe tip	Electron temperature	Electron density	Polytropic index	Features
Sheehan *et al* (2014)	Planar	Simi-log plot of the electron current	Electron saturation current	1.75	Set degree of freedom of 2
Lafleur *et al* (2015)	Cylindrical	Druyvesteyn method	–	1.2–1.55	No distinctive dependence on flow rate
Little and Choueiri (2016)	Cylindrical	Simi-log plot of the electron current	Ion saturation current	1.15	Near isothermal process
Zhang *et al* (2016a)	Cylindrical	Druyvesteyn method		1.17	Adiabatic process (non-local thermodynamic equilibrium)
Takahashi *et al* (2018)	Cylindrical	Druyvesteyn method		1–5/3	Removed axial electric field
Kim *et al* (2018)	Cylindrical	Druyvesteyn method		1–5/3	Spatial variation of polytropic index
Kim *et al* (2019)	Cylindrical	Druyvesteyn method		1–5/3	Spatio-temporal variation of polytropic index
Correyero *et al* (2019)	Cylindrical	Druyvesteyn method		1.23	Spatial variation of polytropic index
Takahashi (2019)	Cylindrical	Druyvesteyn method		1–5/3	Correlation of cross-field diffusion and polytropic index
Kim *et al* (2021a)	Cylindrical	Druyvesteyn method		2	Changes in the degree of freedom by a radial electric field
Kim *et al* (2021b)	Cylindrical	Druyvesteyn method		1.88	Verification of reversible process
Vinci *et al* (2022)	Cylindrical	Simi-log plot of the electron current or Druyvesteyn method	Ion saturation current	1.35–1.85	Two-dimensional measurement of polytropic index

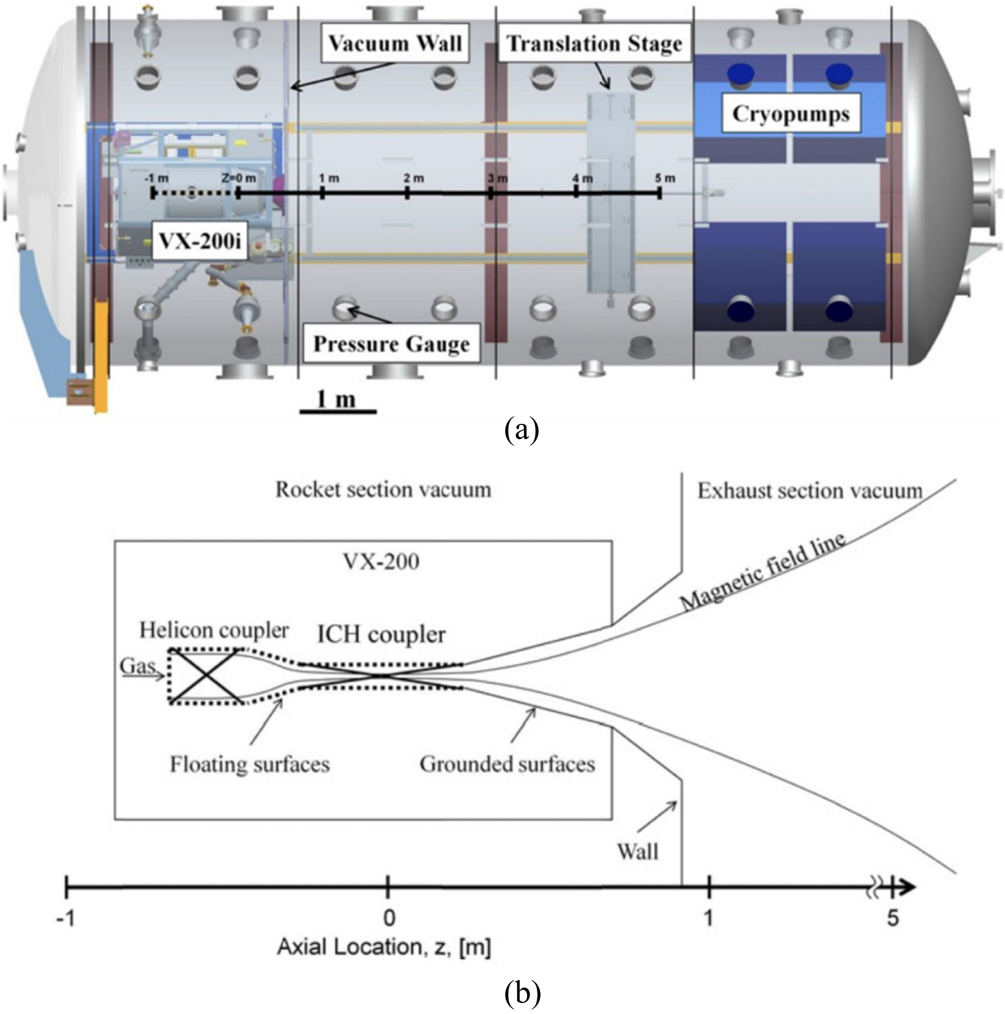

Figure 1. (a) Schematic illustration of the Ad Astra Rocket Company vacuum chamber (overhead view). Reproduced from Longmier *et al* (2011). © IOP Publishing Ltd. All rights reserved. (b) Diagram of the VX-200 device. Reproduced from Sheehan *et al* (2014). © IOP Publishing Ltd. All rights reserved. The ICH coupler shown in (b) was not used in the experiment of (Sheehan *et al* 2014). The operating pressure is almost similar to that of the previous experiments on helicon magnetic nozzles (in the range of 10^{-4} Torr) while a distinctive difference is the size of the vacuum chamber.

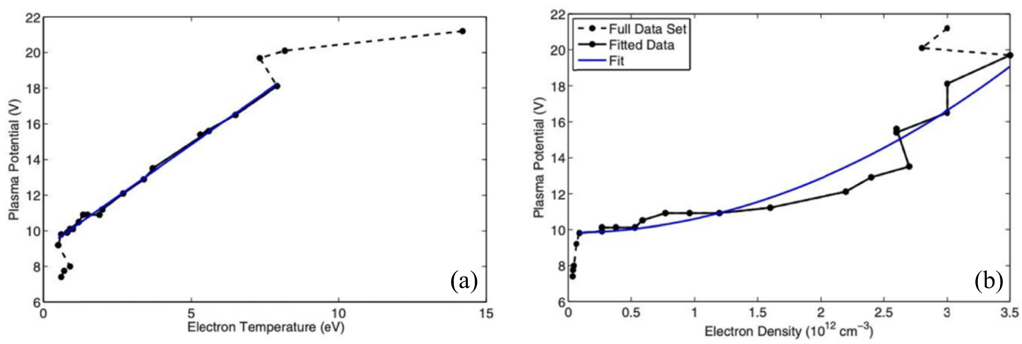

Figure 2. Plasma potential $e\phi$ versus (a) parallel component of electron temperature and (b) density n_e in the magnetic nozzle. The blue lines in (a) and (b) is $e\phi \propto T_{e,\parallel}$ and $e\phi \propto n_e^2$ fit, respectively. The dash lines connecting scattered data points were not included in the fitted data set. Reproduced from Sheehan *et al* (2014). © IOP Publishing Ltd. All rights reserved.

dynamics of the MN, increasing the effective collision frequency and cross-field transport. In this study, detailed experimental and theoretical support for instability and cross-field transport in the MN was not provided. However, in recent years, relevant research has been conducted on a topic related to (Hepner and Jorns 2021) or independent of thermodynamics

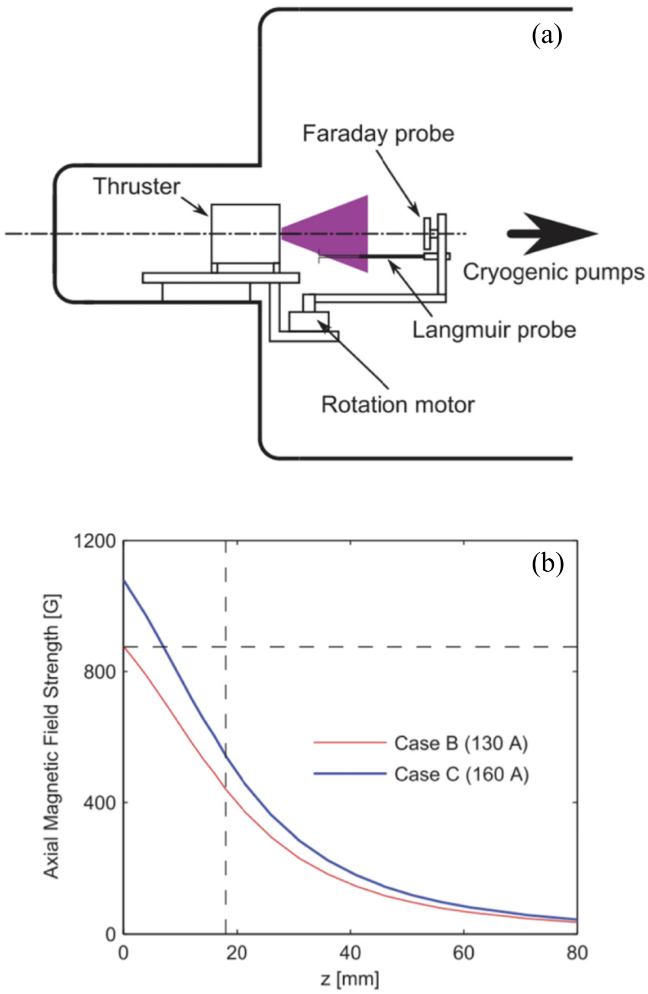

Figure 3. (a) Schematic of electron cyclotron resonance (ECR) plasma thruster and diagnostic apparatus inside the space simulation chamber, and (b) axial profile of the magnetic field strength of the axial component for two cases B and C. The horizontal dash line denotes the magnetic field strength of 875 G at which the ECR is expected to occur. Reproduced from Lafleur *et al* (2015).

(Singh *et al* 2013, Hepner *et al* 2020), and it was revealed that instabilities can increase the turbulent collision frequency of electrons. The enhanced cross-field transport and modification of the EVDF accompanied by the instability is believed to affect the electron cooling physics in the divergent magnetic field. Therefore, we expect that an in-depth discussion can reinforce the contents of the scattered data in the nozzle throat and the far-field region.

The thermodynamic studies conducted in MNs and Hall thrusters have in common that they try to reveal 'the relationship between the heat flux of electrons at the exit of the plasma source and the ion energy' through the combination of the polytropic equation and the momentum equation. Using a similar approach, Lafleur *et al* (2015) suggested the relationship between the maximum ion energy and the electron temperature at the thruster exit plane and the polytropic index. The experimentally observed changes in electron temperature at the nozzle throat and ion energy in the expansion region when the mass flow rate and magnetic field strength are changed [figure 3], and then the polytropic index is estimated.

Experiments were conducted for three electromagnet currents to determine the relationship between the magnetic field, ion acceleration, and electron temperature: case A, no magnetic field; case B, moderate magnetic field (with the ECR condition located at the thruster back wall); and case C, high magnetic field (with the ECR condition located in the center of the thruster). Under null field conditions, surface wave absorption is the dominant heating mechanism in the discharge.

As the magnetic field was strengthened, the electron temperature increased, while the ion energy did not show distinctive changes (figure 4), indicating that the magnetic field does not result in additional ion acceleration in the downstream region. The cooling rate at the electron temperature is larger than that of the ion energy with increasing the magnetic field strength, inferring a proportional relationship between the polytropic index and the magnetic field strength (see figure 5 and equation in the caption). Accordingly, this result provides a perspective that the high cooling rate of the electron temperature far downstream is not directly related to ion acceleration.

As those authors stated, there is room for improvement in the following matters related to measurements in the identification of the electron thermodynamic state. First, as revealed in recent studies, the polytropic index is a value that varies along a divergent magnetic field line (Kim *et al* 2018, Correyero *et al* 2019). From this point of view, the absence of measured data at the nozzle throat, where the 'highest rate of electron cooling' is predicted (positions inside more than 8 cm) suggests the possibility that the (global) measured polytropic index is underestimated. While the Faraday probe is considered a reliable technique for estimating ion energy in plasmas under the assumption of complete expansion at infinity, it is crucial to recognize the importance of local measurements. In a MN within a finite chamber, electron cooling and electric field formation exhibit finite chamber effects. Therefore, to discuss the spatial gradients of the measured plasma variables in conjunction with the ion acceleration mechanism, it is imperative to obtain local measurements of ion velocity capable of observing the finite chamber effect. The anisotropy of the electron temperature is expected to be strong due to the inherent electron heating mechanism of the ECR source, and it should not be overlooked in future studies. Nevertheless, this study is meaningful in that plasma variables are measured and analyzed from a kinetic perspective.

Experiments conducted in a helicon plasma source (Chi–Kung reactor) reported a different thermodynamic state of electrons from previous studies (Zhang *et al* 2016a) [figure 6]. Their logic was based on non-local electron kinetics in the nearly collisionless regime, which focused on the spatial change of the electron energy probability function (EEPF or *eepf*) following the generalized Boltzmann relation.

It was argued that the thermodynamics of electrons in a divergent magnetic field is governed by the non-local EEPF in which the total energy is conserved, and therefore the shape of EEPFs is identical along the axial direction except for the cutting of the low-energy electrons [figure 7]. In this study, EEPFs have a convex structure (Druyvesteyn-like distribution), and

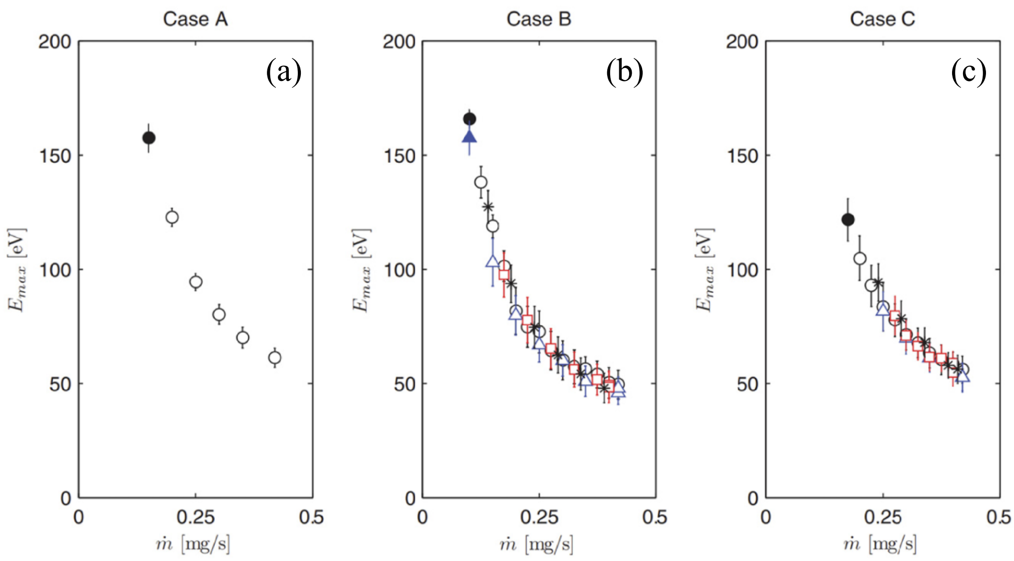

Figure 4. Measured maximum ion energy, $E_{\max}$, as a function of mass flow rate, $\dot{m}$, for (a) case A, (b) case B, and (c) case C. The different symbols and colors of the data show multiple sets of experiments. Reproduced from Lafleur *et al* (2015).

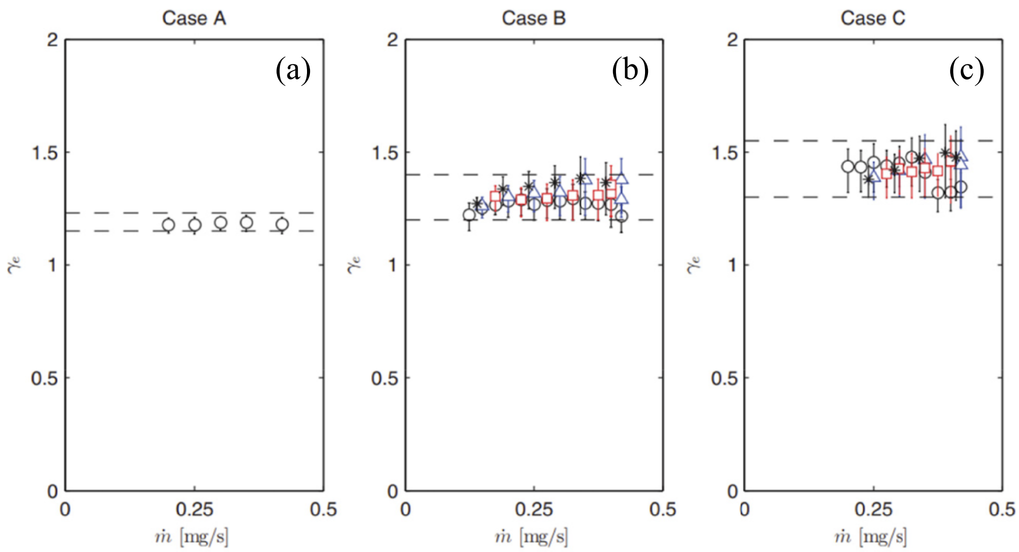

Figure 5. Calculated polytropic index of electrons, γ_e, as a function of mass flow rate, $\dot{m}$, for (a) case A, (b) case B, and (c) case C. The polytropic index is estimated by using the ratio of the maximum ion energy, $E_{\max}$, to the upstream electron temperature, T_{e0}, $E_{\max}/T_{e0}$, as follows; $E_{\max}/T_{e0} = 0.5 + \gamma_e/(\gamma_e - 1)$. The different symbols and colors of the data show multiple sets of experiments. The horizontal dash lines mark the lower and upper limits of the experimental values. Reproduced from Lafleur *et al* (2015).

the calculated effective electron temperature (averaged electron energy) decreases along the axial direction. Accordingly, the electron system does not show dramatic cooling and has a polytropic index of 1.17 closer to the isothermal value. The electrons then transfer their enthalpy into the electric potential energy during the magnetic expansion, verifying an adiabatic process without thermal conduction into the system.

This logic indicates that the polytropic index is dependent on the shape of the non-Maxwellian EEPFs under the condition that the non-local kinetics is dominant (Boswell *et al* 2015). For instance, when the non-local electron kinetics dominates the MN system (total electron energy is conserved), and the shape of EEPFs is concave (bi-Maxwellian-like distribution) with the existence of high-energy groups, the decrease in the electric potential in the axial direction acts as a barrier to the low-energy groups. Thus, the low-energy electrons that cannot overcome the plasma potential decrease in the axial direction, and only electrons with high kinetic energy can reach the far-field. In this case, the effective electron temperature in the far-field region is higher than that of the nozzle

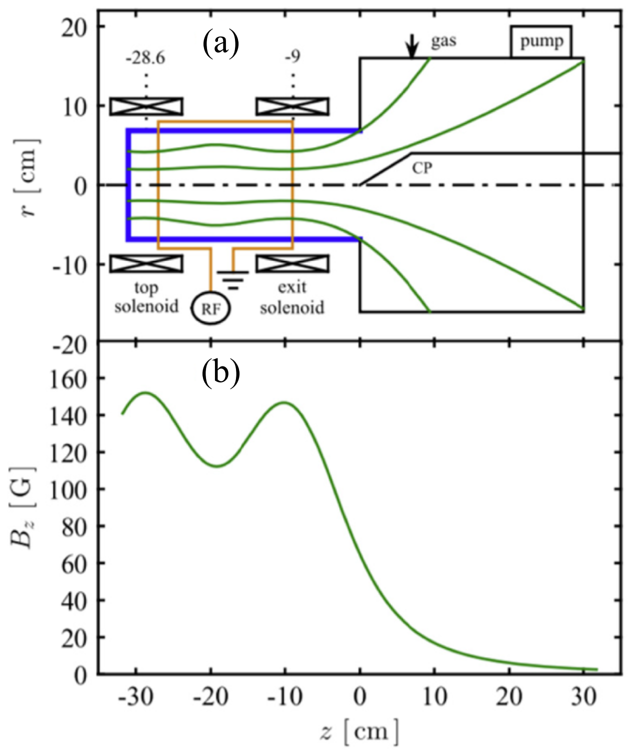

Figure 6. (a) Schematic of Chi–Kung, the helicon plasma reactor, showing the major components, diagnostic probes, and magnetic field lines. (b) Magnetic flux, B_z, on the central axis. Reprinted (figure) with permission from Zhang *et al* (2016a), Copyright (2016) by the American Physical Society.

throat under the identical electric potential structure, indicating that the polytropic index can be less than unity as analyzed by Zhang *et al* (2016b). They concluded that there is a fundamental difference in interpreting the thermodynamics of particles in non-local and local thermodynamic equilibrium, and that the polytropic index closer to unity is not a result of heat conduction along the divergent magnetic field, but rather the result of the non-local properties of electrons along the divergent magnetic field.

We carefully highlight the design factors of the MN (e.g., antenna and magnetic field structure) and the reason for the difference in thermodynamic analysis of each group. Unlike the MN setup of other research groups, a convergent magnetic field line is not clearly observed in the MN with RF sources (Takahashi *et al* 2017a). Eventually, the localized wave heating of electrons near the antenna and its transport along the magnetic field line keeps the electron temperature at the center of the source radius lower than the peripheral radius edge region. As a result, the electron temperature at the radial center at the nozzle throat has a low electron temperature compared to other streamlines of the magnetic field at the same axial location (figure 8(a)). Indeed, the electron temperature of the radial center at the nozzle throat is already closer to that of the outer streamline in the middle of the diffusion chamber, which departs from the plasma source. This phenomenon is also observed in the plasma parameters measured in the ICP nozzle with a double-turn antenna with a large-volume expansion chamber (argon 0.8 mTorr) (figures 8(b)–(d)).

A polytropic index close to 1 regardless of the magnetic field strength and structure was observed in an experiment where the driving pressure was about ten times lower (figure 9) (Little and Choueiri 2016). Interestingly, it is noticeable that the spatial change of the ion energy distribution function (IEDF) is dependent on the magnetic field strength and structure (figure 9). The measured IEDF shows that the ion acceleration slows down in the far-field region as the magnetic current increases (the ion energy has a maximum of about 40 cm at a high magnetic current).

Based on the results of other research groups that the polytropic index can be a function of space, the following analysis is possible. In the linear regression of electron temperature vs electron density, the re-calculated polytropic index of the nozzle throat (eight data in the upper right from the nozzle throat to 18 cm) is 1.23, and thereafter to 30 cm, it is 1.01. When the fitted data set is further reduced (nozzle throat to 7.5 cm), the calculated polytropic index is approximately 1.43, approaching the adiabatic value of 5/3. Although this simple approach has the limitation of providing only phenomenological analysis, the change in the spatial electron cooling rate is a factor to be understood in improving the fundamental understanding of electron thermodynamics and improving the efficiency of MN devices.

2.2. *Effect of trapped electrons*

Previous studies have defined the thermodynamic state of electrons by considering all electrons as a single system. As will be explained in section 4, kinetic models of the plasma expansion (Martinez *et al* 2015, Sanchez-Arriaga *et al* 2018, Merino *et al* 2021) in the MN suggest the existence of three electron subpopulations, occupying different regions of phase space: (1) free electrons coming from the source, and with enough energy to escape to infinity (these electrons are in charge of neutralizing the ion current emanating from the device); (2) reflected electrons coming from the source, and with insufficient energy to escape downstream; and (3) trapped electrons, whose magnetic moment and energy allow them to exist in an intermediate part of the MN, but whose orbits do not connect to the plasma source not to infinity. The studies dealt with in this section subdivide electrons into groups with different thermodynamic states. Such an attempt provides an essential answer to the question of what the thermodynamic state of electrons is in a magnetically expanding plasma.

Takahashi *et al* investigate the thermodynamic state of electrons through a completely different experimental device from previous studies Takahashi *et al* (2018). The newly designed device succeeded in realizing an electric-field-free system by excluding the electric field in the axial direction (figure 10). While this differs substantially from the conditions in a MN, the device can control the plasma potential value and gradient in the axial direction, and consequently, the interaction between magnetic field and electrons can be explored under experimental conditions in which the effect of an axial electric field is completely excluded (figure 11).

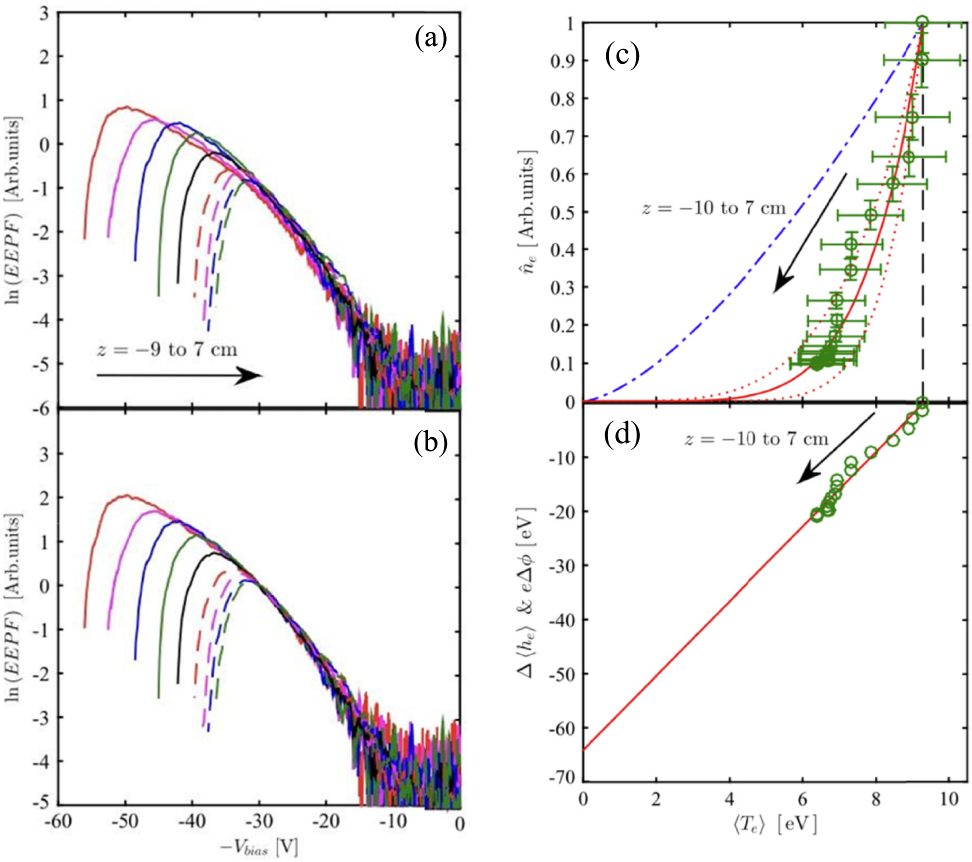

Figure 7. (a) The logarithm of electron energy probability functions (EEPFs) as a function of additive inverse of bias voltage on a single Langmuir probe, $-V_{\text{bias}}$ at each 2 cm from axial location $z = -9$ to 7 cm. (b) EEFPs normalized at $-V_{\text{bias}} = -30$ V. The solid and dash-dotted curves represent the measured EEPFs in the plasma source ($z < 0$ cm) and diffusion chamber ($z > 0$ cm), respectively. (c) Correlation data between normalized electron density, $\hat{n}_{\text{e}}$, and effective electron temperature, $\langle T_{\text{e}} \rangle$. A polytropic curve with an index of 1.17 is plotted as a red solid curve. The upper and lower limit curves around the polytropic curve given as two dotted lines are obtained by fitting the experimental parameters. The dash-dotted line (red) and dash line (black) represent the processes with a polytropic index of 5/3 and unity, respectively. (d) Relative electron enthalpy, $\Delta\langle h_{\text{e}} \rangle$ (solid line), and relative plasm potential, $\Delta\phi$ (open circles), as a function of $\langle T_{\text{e}} \rangle$. The electrons transfer their effective enthalpy into potential energy during the plasma expansion. See Zhang *et al* (2016a) for a detailed explanation. Reprinted (figure) with permission from Zhang *et al* (2016a), Copyright (2016) by the American Physical Society.

When the potential difference is close to zero and the change in the axial direction is negligible, the electron temperature is rapidly cooled along the magnetic field, and the measured polytropic index is greater than 1.4, approaching the adiabatic value of 5/3 (figures 11 and 12). On the other hand, when the potential difference is large and an electric field in the axial direction is formed, like a general MN, the thermodynamic state of electrons is close to isothermal. The study suggests that when the generation of trapped electrons by the electric field is suppressed, the electron system can work in the magnetic field alone, and the Lorentz force generated by the non-uniformity of the radial plasma density acts on the expanding magnetic field to form an ideal gas that expands adiabatically (figure 11). This causes a decrease in the internal energy of the working electron. This means that the classical laws of thermodynamics can be extended to the expansion of a collision-free electron gas in a MN.

While the Takahashi *et al* study emphasized that only electron groups that undergo adiabatic expansion can be observed when the electric field is artificially removed, Kim *et al* independently carried out experiments that observe the thermodynamic state of each electron group in a MN in the presence of an axial electric field Kim *et al* (2018). They analyzed the electron thermodynamics under the perspective that a magnetic mirror formed by the combination of magnetic field and self-generated electric field can create a trapped electron motion. A double-sided planar Langmuir probe is used to selectively collect electron groups in the expansion region of the MN device.

The presence of isothermally behaving electrons separates the MN system into two regions with different thermodynamic properties (figure 13). One is an adiabatic region located near the nozzle throat and the other is an isothermal region located downstream. In this region separation effects are maximized when the strength of the magnetic field is increased. At high magnetic field strength, an abrupt change in effective electron temperature is observed at the nozzle throat by the front side of the probe (downward probe), and the calculated polytropic index is closer to 5/3. On the other hand, when the strength of the magnetic field is weak, the decrease rate of electron

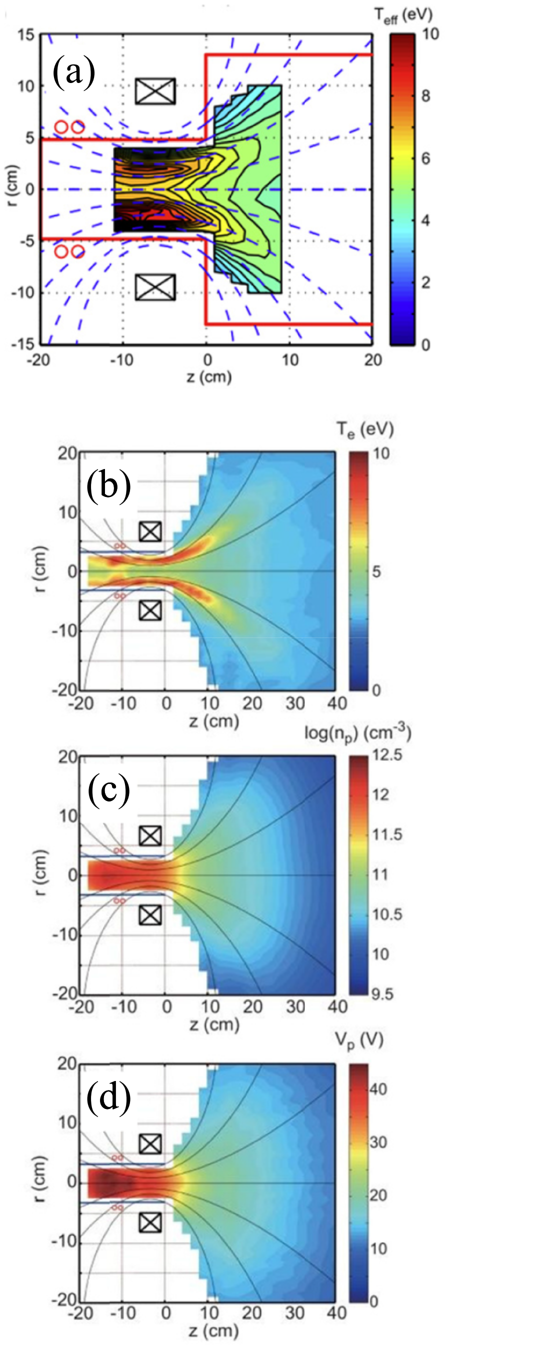

Figure 8. Two-dimensional profiles of the electron temperature, T_e, measured in (a) small (26 cm diameter and 30 cm long) and (b) large (60 cm long and 140 cm long) diffusion chambers, respectively. A Pyrex source tube of 6.4 cm inner diameter and 20 cm long and 9.4 cm inner diameter and 20 cm long is immersed in each small and large diffusion chamber, respectively. (c) The logarithm of the plasma density, $\log n_p$, and (d) the plasma potential, V_p, for the setup of a large diffusion chamber are depicted. Compared to the large radial gradient of electron temperature, the relatively uniform density and plasma potential in the radial direction of the source region are impressive. Reprinted from Takahashi *et al* (2017a), with the permission of AIP Publishing.

temperature becomes lower, and the polytropic index calculated by measured EEPFs by the downward probe has a value closer to unity in the entire area of the nozzle. Interestingly, the upward probe (back probe) only collects non-locally behaving low-energy electrons showing an isothermal polytropic index.

The change in the thermodynamic properties of electrons varying with the strength of the magnetic field can be well explained by the spatial formation of the maximum magnetic moment. As the magnetic field strength increases, the bounce region of electrons (maximum magnetic moment well) moves to the far region of the MN. In other words, a polytropic index close to 5/3 is regarded as the result of a shift in the bounce region where the cooled electrons stagnate (figure 14).

Importantly, the studies of Kim and Takahashi provided experimental consensus on the different polytropic indexes found in each study group. The spatial distribution of two-electron groups with different thermodynamic states determines the polytropic index, and the properties of electric and magnetic fields possessed by the devices in each group have a polytropic index ranging from 1 to 5/3. Ultimately, this study demonstrates that a single value of the effective polytropic index cannot be attributed to all MNs.

Previous thermodynamic studies have been limited to static observations of plasmas that have reached a steady state, and time-dependent kinetic analysis successfully identified a series of electron cooling processes in a MN (Kim *et al* 2019). By controlling the diffusion of the source plasma into the expansion region using a mesh grid installed at the boundary of the source and expansion region (figure 15), a series of electron cooling, generation of the ambipolar electric field, and the production of trapped electrons could be observed. The gradually accumulated electrons change the low energy of the EEPFs (figure 16). The accumulation of trapped electrons reduces the degree of cooling of the system, and the electric field initially generated by the adiabatic expansion in the downstream region disappears due to disconnection from the source.

The log–log relationship of data shows that the adiabatic process dominates the electron thermodynamics near the nozzle throat at all moments (figure 17). That is, the thermodynamic states of the electrons near the nozzle throat are maintained over time. Up to 3.0 ms, the slope of the log–log plot (i.e. the polytropic index) does not change during the entire expansion region. In contrast, a temporal variation of the slope is observed in the far-field region. The evaluated polytropic index is closer to unity as it approaches the downstream, indicating that the gradually accumulated, trapped electrons in the downstream region behave to preserve the thermal energy with time. This study suggests the fundamental cause of the spatially varying polytropic index, emphasizing that the consideration of the trapped electrons is an essential factor for understanding the characteristics of a magnetically expanding plasma.

2.3. Changes in the degree of freedom

Generally, in the experiments and modeling performed on the MN device, the electron degrees of freedom were set to 1 and 2 in the parallel (axial motion) and perpendicular (radial and azimuthal motion) to magnetic field lines in cylindrical coordinates, respectively. Accordingly, the adiabatic limit of the polytropic index would correspond to 5/3 in the MN.

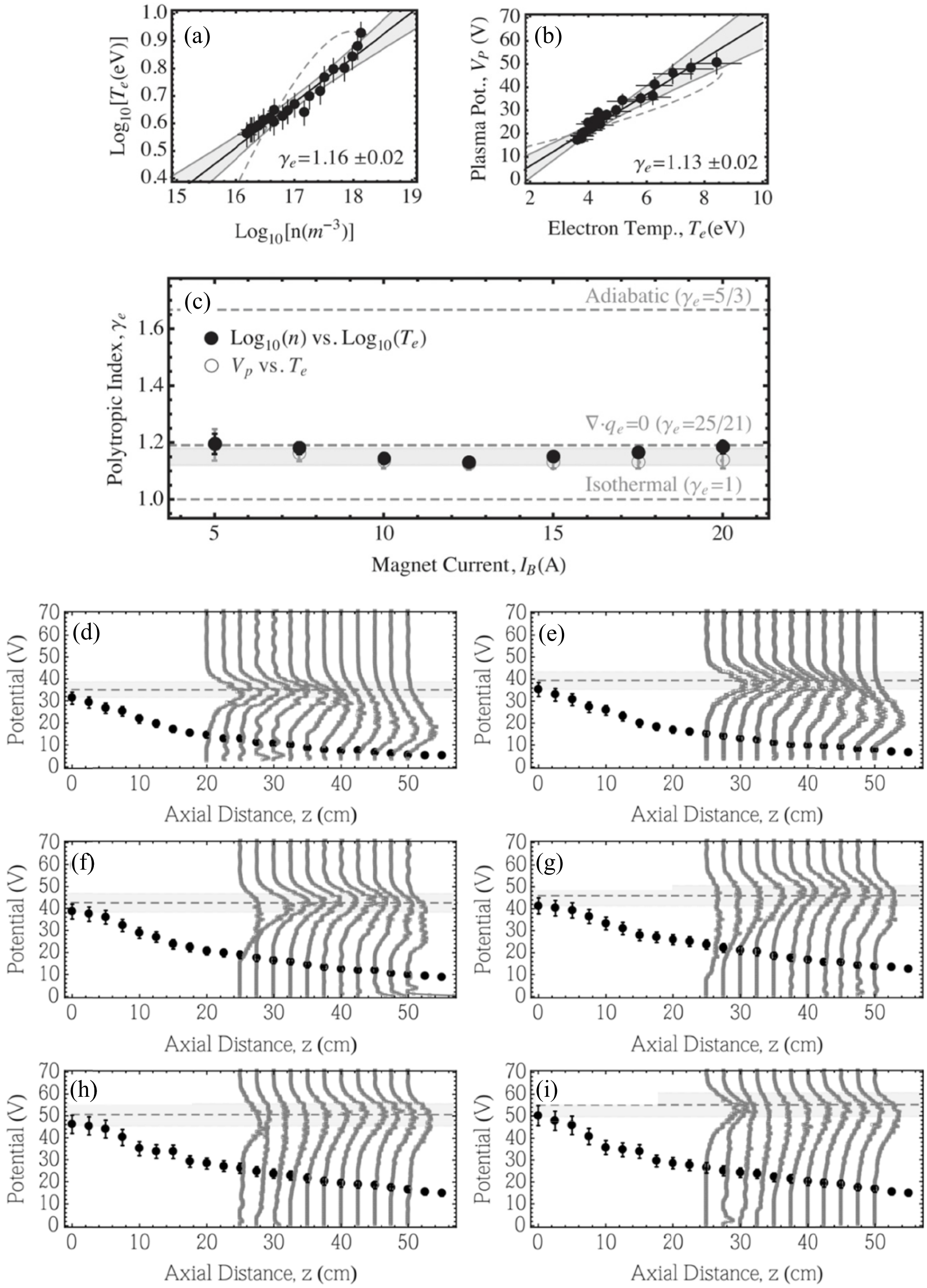

Figure 9. Estimation of the polytropic index, γ_e, with experimental measurements of electron temperature, T_e, electron density, n, and plasma potential, V_p, with the relation of (a) $\log T_e$ versus $\log n$, and (b) V_p versus T_e. The solution to the quasi-1D model is also shown (dashed line). The polytropic index is determined using the method of least squares (line). (c) The dependency of γ_e on the magnet current, I_B, is shown (c). The axial evolution of the ion energy distribution function and V_p with varying I_B of (d) 5.0 A, (e) 7.5 A, (f) 10.0 A, (g) 12.5 A, (h) 15.0 A, and (i) 17.5 A. Reprinted (figure) with permission from Little and Choueiri (2016), Copyright (2016) by the American Physical Society.

Interestingly, it was found that the control of the degrees of freedom in the MN device was made possible through the reduction of cross-field transport via the radial electric field (Takahashi *et al* 2018, Kim *et al* 2021a). The strengthening of the radial electric field was achieved through the increase in the magnetic field strength, and it was eventually proved that the reduced degree of freedom increases the electron cooling rate (polytropic index). Ultimately, the essence of the relationship between degrees of freedom and electron thermodynamics can be understood by controlling the following variables: (1)

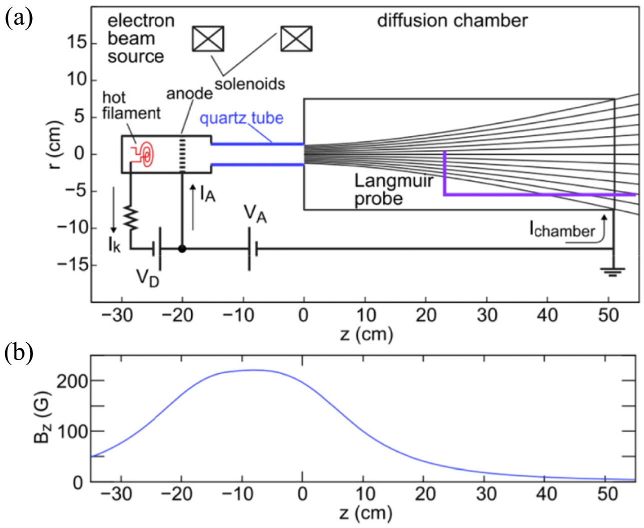

Figure 10. (a) Schematics of the experimental setup. (b) The axial profile of the magnetic field along the axis. In the specially designed setup, the plasma potential is mainly governed by the anode potential, which is an intrinsic characteristic of the DC plasma sources. Reprinted (figure) with permission from Takahashi *et al* (2018), Copyright (2018) by the American Physical Society.

strengthening the radial electric field and restricting the cross-field transport of plasma and (2) eliminating the axial electric field to prevent the electrons from trapped motion along magnetic field lines. To minimize the axial electric field and maximize the radial electric field, a DC filament plasma source is installed in the source region where the plasma potential is determined by the anode potential; the grounded chamber wall is designated as the anode, thus, the plasma potential is closer to zero (Kim *et al* 2021a). Since the cross-sectional area of the expanding beam-plasma (which is dominated by the size of the filament in the source region) is excessively smaller than the expansion region, the radial electric field is generated in the expansion region. The aforementioned electric field formation is an intrinsic property of DC or indirectly heated cathode discharges that generate beam-plasma (Kim *et al* 2021c).

The strength of the magnetic field was changed by controlling the current of the nozzle field coil, and the gradient scale length of the magnetic field was changed through an additional guiding coil to change the structure of the magnetic field (figure 18).

Although the strength and structure of the magnetic field were changed, the plasma potential structure in the axial and radial directions were kept constant, while the electron temperature and density gradient were different in each experimental condition (Kim *et al* 2021a). Nevertheless, the fixed electric field strength regardless of the magnetic field properties ensures the invariance of the polytropic index closer to 2, indicating the reduced degree of freedom to 2 (figure 19).

The change of the polytropic index due to cross-field diffusion was proposed in an earlier study by Takahashi *et al* (2020a), but they did not introduce the concept of degrees of freedom. Takahashi *et al* pointed out the limitations in that studies on the investigation of electron thermodynamics in MN devices focused only on axial plasma variables and provided a new perspective based on the radial variation of plasma parameters. When the magnetic field strength is increased, both the magnetization of the electrons and the electric field confining the ions are radially enhanced; the polytropic index approaches the adiabatic value of 5/3 (figure 20). When the direction of the electric field is toward the radial center, and the strength was sufficient to confine the ions, this effect limits the cross-field transport of electrons. Based on these experimental results, they identified the dependence on the magnetic field strength and the thermodynamic state of electrons; the polytropic index becomes dependent on (and proportional to) the magnetic field strength.

It turns out that if the magnetic field strength becomes stronger in their experiments to completely limit the cross-field transport of electrons and ions in the radial direction, the polytropic index is close to 2. That is, as in Kim's study, when a sufficient radial electric field is ensured, it is expected that the polytropic index of an adiabatic value is 2 due to the reduced degrees of freedom of electrons regardless of the strength and structure of the magnetic field.

Finally, we discuss the evolution of EEPFs during the adiabatic process in a divergent magnetic field. Interestingly, the measured evolution of EEPFs is close to the Maxwellian distribution function at the nozzle throat, while the non-Maxwellian EEPFs are prominent in the far-field region of the MNs (figure 21).

The explanation for this phenomenon was clarified by the adoption of non-extensive thermodynamics (Kim *et al* 2021b). In the MN device, the EEPFs can be fitted through the kappa function (figure 22). Currently, it has been revealed that the cooling of electron temperature and the maintained kappa values along the expanding magnetic field represent a *reversible* and *adiabatic* process, respectively (figure 23). This indicates that the changes in non-Maxwellian EEPFs along the divergent magnetic field are an inevitable result of the thermodynamic process. The interpretation of the study can be extended to determine whether electrons with a non-Maxwellian distribution satisfy the laws of thermodynamics. By introducing non-extensive statistical mechanics, they found an answer to the fundamental question of whether collisionless, magnetically expanding, non-equilibrium electrons satisfy the laws of thermodynamics via non-extensive Tsallis entropy.

Various experimental studies to understand the cooling of electrons in MN devices have been summarized. The study of electron thermodynamics has been extended to consider the relationship between the trapping of electrons, the cross-field diffusion, and the degrees of freedom of electrons with a polytropic index. As the research that started with a general device to generate ion beams was subdivided into basic physical research using filament sources, it was possible to separate and observe electron groups with different thermodynamic properties, and finally suggest the following main points. The adiabatic expansion of electrons contributes to the formation of an electric field, which contributes to the creation of various groups of electrons, including trapped electrons. Therefore, in order to understand the physics of MN devices and to suggest engineering directions for performance improvement, it

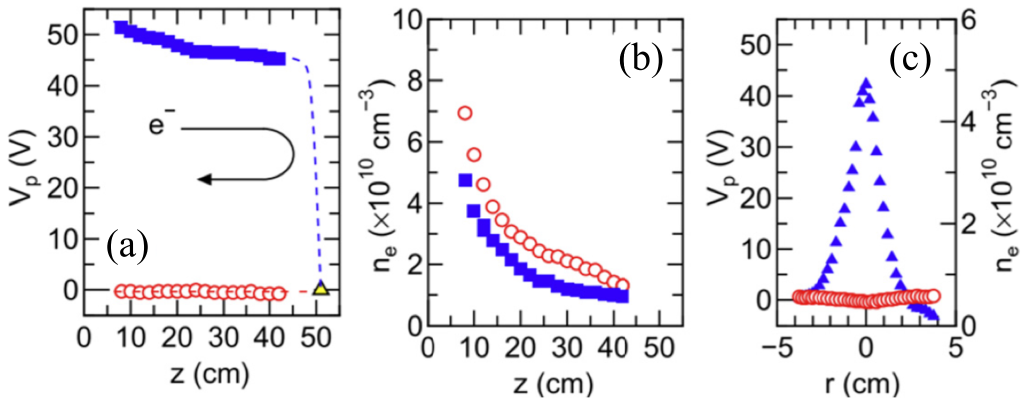

Figure 11. (a) The axial profile of the plasma potential, V_{p}, for anode potential, V_{A}, of 60 V (filled squares) and 0 V (open circles). The triangle shows a grounded wall potential at the axial location, z, of 51 cm. (b) Axial profile of electron density, n_{e}, for the same values of V_{A}. (c) Radial profiles of V_{p} (open circles) and n_{e} (filled triangles) measured at $z = 10$ cm for $V_{\mathrm{A}} = 0$ V. Reprinted (figure) with permission from Takahashi *et al* (2018), Copyright (2018) by the American Physical Society.

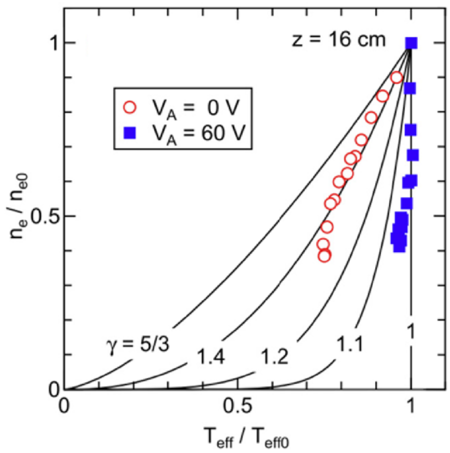

Figure 12. Polytropic relations are obtained from the measured electron energy probability functions, together with the theoretically calculated curves with spatially varying electron density, n_{e}, and effective electron temperature, T_{eff}, normalized by the center value. Reprinted (figure) with permission from Takahashi *et al* (2018), Copyright (2018) by the American Physical Society.

is essential to group electrons with distinct dynamic and thermodynamic characteristics in electric and magnetic fields.

3. Theoretical approach to electron thermodynamics

The initial study of MNs was accomplished with paraxial fluid models (Andersen *et al* 1969, Kuriki and Okada 1970, Sercel 1990). These simple models prescribed an isothermal or polytropic law for the electron thermodynamics and were able to satisfactorily explain the main aspects of the first experiments on MNs. Paraxial models continue to be proposed to analyze some aspects of the plasma expansion (Fruchtman *et al* 2012). Two-dimensional models opened the way to investigate the radial dynamics of the plasma in the MN, as well as the distribution of azimuthal electron currents and their role in the operation of the device and plasma detachment (Hooper 1993, Winglee *et al* 2007, Breizman *et al* 2008); Nevertheless, Hooper (1993) artificially tied ion and electron trajectories, while Breizman *et al* (2008) missed the central role of electron thermal energy in the plasma expansion; hence, these two arrived at partially wrong conclusions on aspects such as thrust generation and detachment.

Part A of this section reviews in particular the 2D two-fluid model of (Ahedo and Merino 2010, Merino and Ahedo 2016a) as a framework to explain the key aspects of MN plasma expansions. This framework has been successful in explaining the fundamentals of the operation of MNs (ion acceleration, magnetic thrust generation and azimuthal electric currents (Ahedo and Merino 2010), effects of collisions and electron inertia (Ahedo and Merino 2012), formation of double layers in the presence of two-temperature electron distributions (Ahedo and Martinez-Sanchez 2009, Ahedo 2011b, Merino and Ahedo 2013), plasma detachment (Merino and Ahedo 2014), effects of ion temperature (Merino and Ahedo 2015), effects of the plasma-induced magnetic field (Merino and Ahedo 2016b), and contactless thrust vectoring (Merino and Ahedo 2017). The 2D model uses a simple, empirical isothermal or polytropic closure relation for the electron species, and therefore it renounces to analyze the causes leading to electron cooling and temperature anisotropy, which is left for part B of this section.

The study of electron cooling, anisotropization, and thermodynamics in the MN using kinetic models has occurred in parallel in the last decades. Full particle-in-cell simulations and semi-analytic methods have been used to this end. Hu and Wang (2015) employed a full particle-in-cell approach to electron kinetics in the plasma plume expansion. While they recover interesting trends in electron cooling and anisotropy, their work is limited by the downstream boundary conditions used, which cause a numerical instability when electrons start reaching it. Hence, they limit the simulation time to a short transient. Recent work by Li *et al* (2019) developed new boundary conditions for particle-in-cell codes

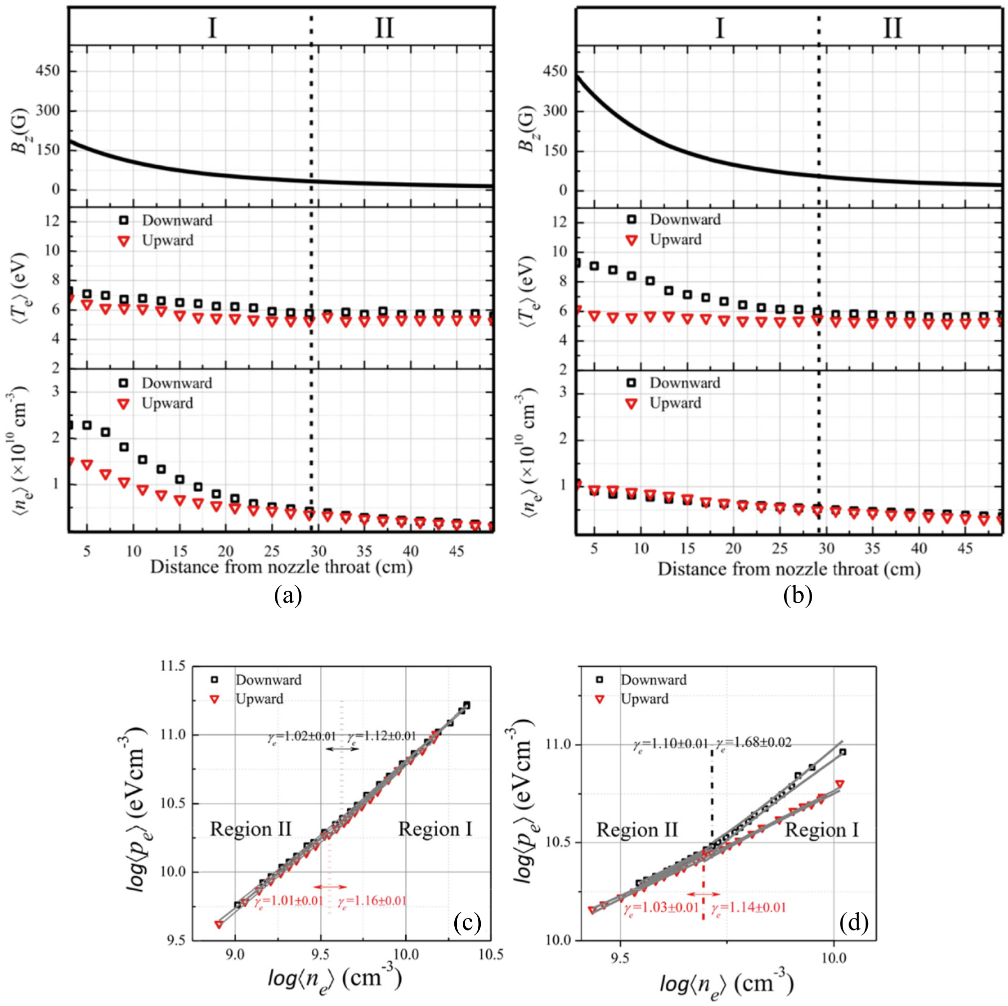

Figure 13. The axial profile of magnetic flux, B_z, and electron parameters are measured by the front probe (open squares) and back probe (open triangles) from 3 to 49 cm from the nozzle throat at (a) 50 A, and (b) 200 A of the electromagnetic current: effective electron temperature, $\langle T_e \rangle$, electron density $\langle n_e \rangle$. A log-log relationship between the effective electron pressure $\langle p_e \rangle$ and $\langle n_e \rangle$ averaged over 1D electron energy probability functions is obtained at 2 cm intervals from 3 to 49 cm from the nozzle throat. The polytropic index of the MN system is determined by a combination of thermodynamic properties of isothermal and adiabatic electron groups, showing (c) the isothermal behavior at 50 A and (d) the coexistence of adiabatic and isothermal groups near the nozzle throat and its evolution into the isothermal at the far-field region at 200 A. Reproduced from Kim *et al* (2018).

that prevent this artifact and enable the simulation until a steady state is reached. Andrews *et al* (2022) have introduced a variant of this new boundary condition. Their study of the MN shows a piecewise, three-polytropic population of electrons, whose indices depend axially on the degree of magnetization.

Arefiev and Breizman (2008) established a 1D model that takes into account the combined effect of the electric field and the magnetic mirror effect, distinguishing between 'coupled' electrons and 'uncoupled' electrons. By invoking a transient rarefaction wave at the front of the expansion, they are able to compute the EVDF of uncoupled electrons, assuming that the axial bouncing of electrons at the rarefaction wave has an associated adiabatic invariant. While this model introduces many of the necessary concepts to understand the kinetic expansion of electrons in a MN, it leaves out free electrons and empty regions in phase space, and thus it is unable to correctly determine the electric potential fall in the expansion, $\phi_0 - \phi_\infty$, and its relation to the current-free condition that a MN must satisfy.

Martínez-Sánchez *et al* (2015) developed a semi-analytical model that takes free electrons into account, yielding valid values for the odd-moments of the electron distribution function. Part B covers, in particular, this and subsequent derived developments in detail. First, a steady-state, collisionless model is discussed that manifests the existence of distinct electron subpopulations (free, reflected, and doubly-trapped electrons) (Martinez-Sánchez *et al* 2015, Ramos *et al* 2018, Ahedo *et al* 2020, Merino *et al* 2021). Then, a time-dependent model is reviewed that is able to recover the filling of the trapped electron phase space via the initial transient set-up process of the plume (Sánchez-Arriaga *et al* 2018) and via collisions (Zhou *et al* 2021). Conclusions drawn from these models, as well as their limitations and pending work, are also discussed.

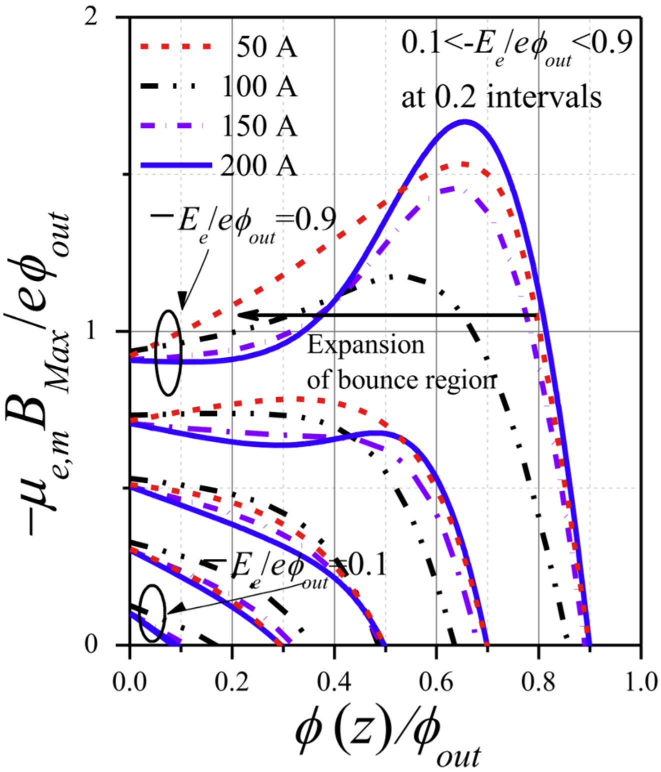

Figure 14. For electrons, the local maximum magnetic moment $\mu_{\mathrm{e,m}}\left(z,E_{\mathrm{e}}\right)$ with total energy E_{e} is expressed as follows: $\mu_{\mathrm{e,m}}\left(z,E_{\mathrm{e}}\right)=\left(E_e+e\phi\left(z\right)\right)/B_z$. The local maximum magnetic moment has minimum and maximum values at points, which eventually clarifies the bounce motion of electrons in a MN system. The confined electrons having energy below the total potential drop then bounce back (reflected and trapped electrons) and forth (trapped electrons) in the bounce region. The graph shows the normalized local maximum magnetic moment $-\mu_{\mathrm{e,m}}B_{\mathrm{Max}}/e\phi_{\mathrm{out}}$ versus normalized plasma potential drop $\phi\left(z\right)/\phi_{\mathrm{out}}$ for various normalized electron energies at the nozzle current increasing from 50 to 200 A. Reproduced from Kim *et al* (2018). © IOP Publishing Ltd. CC BY 3.0.

3.1. Two-fluid framework of magnetized plasma expansions in space

In the following, we restrict ourselves to an electron-driven, divergent, axisymmetric MN, in which electrons are warm and ions are cold, except where otherwise noted. Under the assumption that the plasma in the MN is collisionless and quasineutral and composed of fully magnetized electrons and partially magnetized, cold ions, the steady-state expansion is described by the following continuity and momentum equations:

$$\nabla\cdot\left(n\boldsymbol{u}_i\right)=0, \tag{1}$$

$$m_i\boldsymbol{u}_i\cdot\nabla\boldsymbol{u}_i=-e\nabla\phi+e\boldsymbol{u}_i\times\boldsymbol{B}, \tag{2}$$

$$\nabla\cdot\left(nu_{\|\mathrm{e}}\mathbf{1}_{\|}\right)=0, \tag{3}$$

$$0=-\nabla\cdot\overline{\overline{P}}_{\mathrm{e}}+en\nabla\phi-enu_{\theta\mathrm{e}}B\mathbf{1}_{\perp}, \tag{4}$$

where the electron bulk velocity has been written as

$$u_{\mathrm{e}}=u_{\|\mathrm{e}}\mathbf{1}_{\|}+u_{\theta\mathrm{e}}1_{\theta},u_{\perp\mathrm{e}}=0, \tag{5}$$

and $\left\{\mathbf{1}_{\|},\mathbf{1}_{\perp},\mathbf{1}_{\theta}\right\}$ is a right-handed, magnetically aligned vector basis, with $\mathbf{1}_{\|}=\boldsymbol{B}/B$ and $\mathbf{1}_{\perp}$ in the meridian plane. All symbols above are conventional. Observe that equations (4) and (5) retain zeroth-order Larmor radius effects only, and in particular, equation (4) disregards electron inertia, which is negligible compared to ion inertia.

To close the fluid equation hierarchy at this level (i.e., without involving the energy equation), the pressure tensor $\overline{\overline{P}}_{\mathrm{e}}$ is assumed to be isotropic so that $\nabla\cdot\overline{\overline{P}}_{\mathrm{e}}=\nabla p_{\mathrm{e}}$, and moreover, a closure relation for the scalar pressure of the polytropic form

$$p_{\mathrm{e}}\propto n^{\gamma} \tag{6}$$

is imposed, with the polytropic coefficient γ an empirical constant. Observe that $\gamma=1$ yields the isothermal limit, while $\gamma=5/3$ is the adiabatic value for electrons with 3 degrees of freedom.

This closure has the additional advantage that equation (4) can be integrated in the parallel direction, yielding:

$$H_{\mathrm{e}}=\frac{\gamma}{\gamma-1}T_{\mathrm{e}0}\left[\left(\frac{n}{n_0}\right)^{\gamma-1}-1\right]-e\phi \tag{7}$$

(for $\gamma\neq1$), where $T_{\mathrm{e}0}$ and n_0 are reference upstream values of the electron temperature and plasma density, respectively. The integration constant H_{e} is magnetic line-dependent and can vary across lines. In fact, H_e is fully determined from the conditions at the magnetic throat, which is the section of maximum magnetic field strength.

Then, taking the perpendicular projection of (equation (4)), we find

$$u_{\theta\mathrm{e}}=-\frac{\mathbf{1}_{\perp}\cdot\nabla H_{\mathrm{e}}}{eB}. \tag{8}$$

which provides the azimuthal electron velocity along the MN given the field strength B and the value of H_{e} upstream.

Expression (7) can be used to eliminate ϕ in the ion equations (1) and (2), which then become analogous to the Euler gas dynamics equations with the pressure provided by the electrons, and extra source terms due to the magnetic force on the plasma,

$$\mathbf{F}_{\mathrm{M}}=eB\left[\left(u_{\theta i}-u_{\theta\mathrm{e}}\right)\mathbf{1}_{\perp}-u_{\perp i}1_{\theta}\right]. \tag{9}$$

The ion flow undergoes a sonic transition at the magnetic throat. The hyperbolic differential equations for the supersonic ion flow in the divergent part of the MN can be solved for $\boldsymbol{u}_i$ and n with common techniques (method of characteristics, finite volumes, discontinuous Galerkin, etc). Finally, the electron continuity equation (3) can be used to compute $u_{\|\mathrm{e}}$, as electron streamtubes coincide with magnetic streamtubes.

Ahedo and Merino (2010) and Merino and Ahedo (2013) contain a detailed account of the dynamics of this system, including ion acceleration and thrust generation mechanisms. The main driver of the expansion is the electron thermal

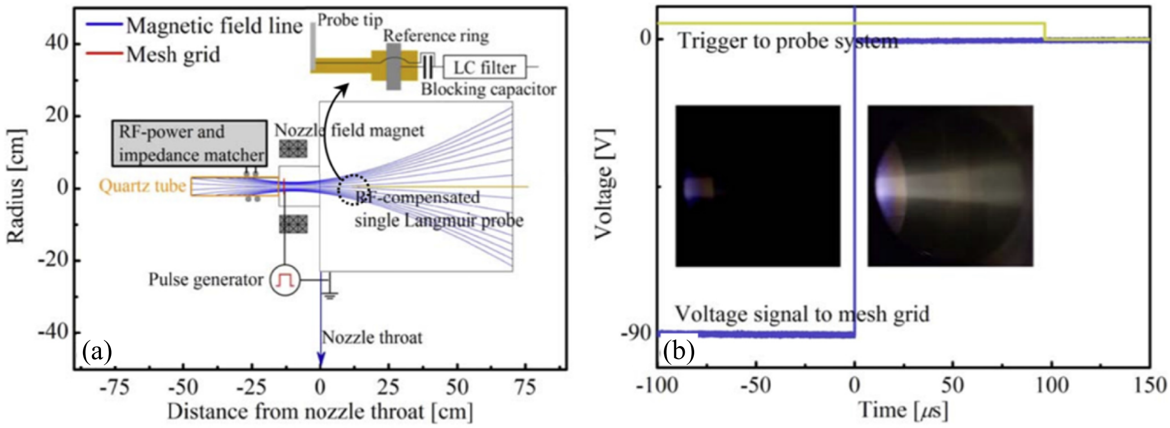

Figure 15. The schematic diagram of (a) the magnetic nozzle device driven by the inductively coupled plasma source and the divergent magnetic field configuration. An axially movable RF-compensated single Langmuir probe is located at the expansion region. In order to observe a series of electron expansion, a mesh grid is installed at -13 cm from the expansion chamber throat, and (b) the voltage signal to the mesh grid and trigger to probe system (the internal images, which were taken under steady-state conditions at each voltage, are inserted to aid the understanding of the experiment). Reproduced from Kim *et al* (2019).

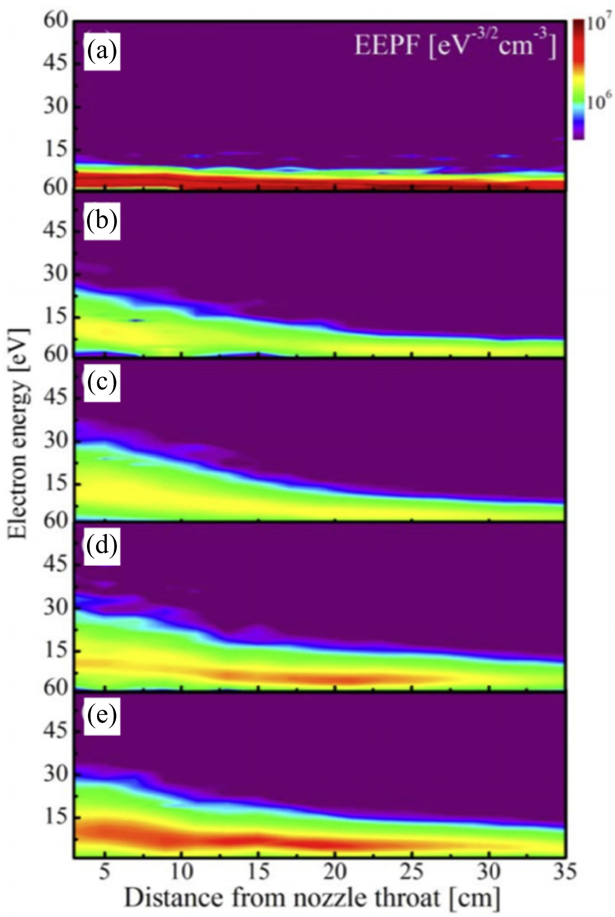

Figure 16. Time evolution of the electron energy probability functions (EEPFs) at (a) -0.5 μs, (b) 3.0 μs, (c) 7.5 μs, (d) 25 μs, and (e) 95 μs relative to the beginning of the pulse rise time (0 μs). Reproduced from Kim *et al* (2019).

energy. In an unmagnetized plasma plume, the parallel thermal energy of electrons is converted to the directed kinetic energy of ions thanks to the electrostatic potential. This is referred to as ambipolar acceleration. The main advantage of the MN, however, is the following: the perpendicular electron thermal energy, which would be wasted in the absence of a guiding magnetic field, is converted to parallel electron thermal energy. This energy is then available for the continued acceleration of ions.

The force that converts the perpendicular to parallel energy is the magnetic force on the electron fluid,

$$F_{\mathrm{Me}} = eBu_{\theta\mathrm{e}}\mathbf{1}_{\perp} \equiv -\left(\mathbf{1}_{\perp}\cdot\nabla H_{\mathrm{e}}\right)\mathbf{1}_{\perp}, \tag{10}$$

and is the largest term in expression (9). The reaction to this force is felt on the magnetic circuit that generates the MN; the parallel component of this reaction is termed (electron) *magnetic thrust*. Positive magnetic thrust results from electric currents in the plasma that induce a magnetic field that opposes the applied one (i.e., diamagnetic currents). In standard MNs, the function H_{e} at the throat decreases radially, and the electron azimuthal current is always and everywhere diamagnetic (i.e., thrust producing). This is so even if part of the azimuthal electron current downstream is due to the $\boldsymbol{E}\times\boldsymbol{B}$ drift, which under usual conditions is paramagnetic (i.e., drag producing).

The remaining terms in expression (9), due to the ions, can be diamagnetic or paramagnetic. For initially non-rotating ions (i.e., zero ion swirl at the throat), the magnetic force on ions is zero initially, and rather small but paramagnetic downstream.

The magnetic force on electrons, F_{Me}, scales with H_{e}, which in turn scales with T_{e0} and depends on the cooling rate γ. Consequently, so does the ion momentum gain and the magnetic thrust produced by the MN. Figure 24 shows the computed in-plane ion velocity in a MN with polytropic ($\gamma = 1.3$) and isothermal ($\gamma = 1$) electrons, where the differences are evident. It is therefore paramount to determine the thermodynamics of the electrons in the collisionless MN expansion, and in particular, the electron cooling, to evaluate the performance of the device, including the magnetic thrust.

As a side note, we observe that in MNs with warm or hot ions, the ion thermal energy is also a driver of the

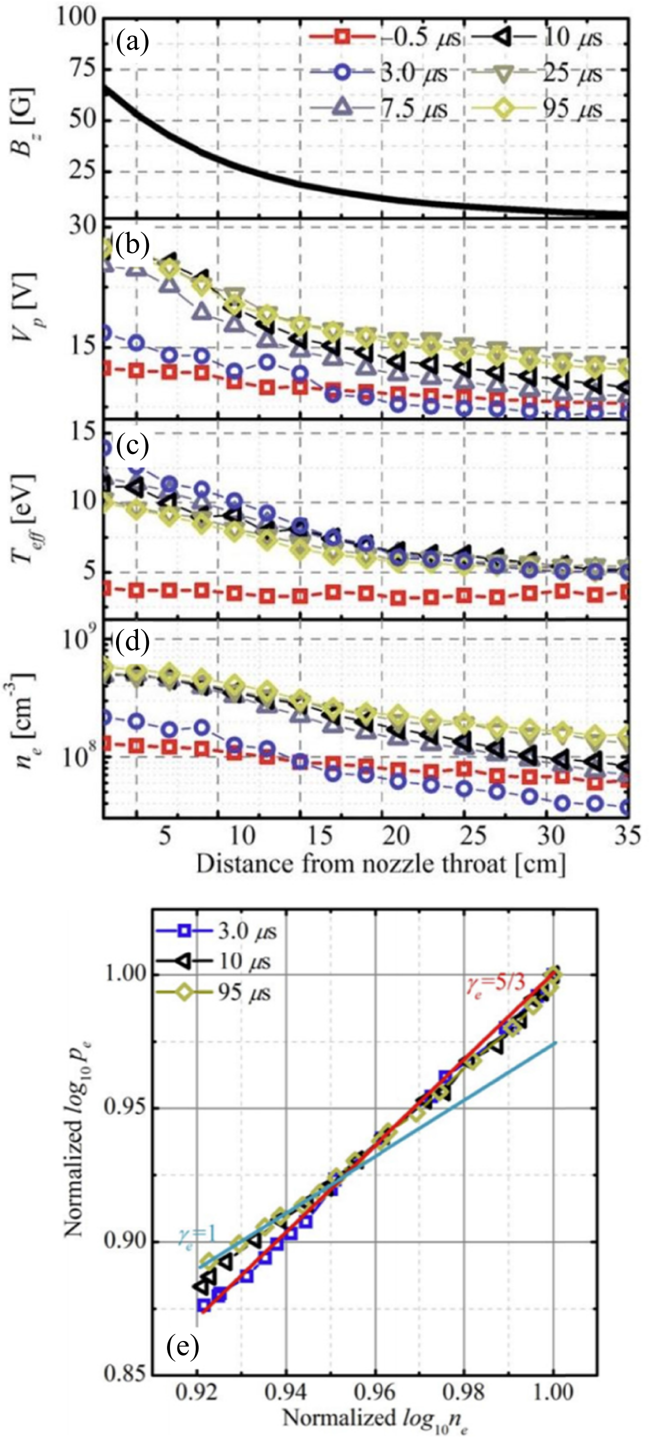

Figure 17. The axial profile of (a) the magnetic flux, B_z, and that of the electron parameters from 3 to 35 cm from the nozzle throat over time, (b) the plasma potential, V_p, (c) the effective electron temperature, T_{eff}, and (d) the electron density, n_e. (e) Log–log relationship between the effective electron pressure p_e and n_e. Polytropic curves with an exponent of 5/3 (solid red) and unity (solid blue-green) represent the adiabatic and isothermal processes, respectively. Reproduced from Kim *et al* (2019).

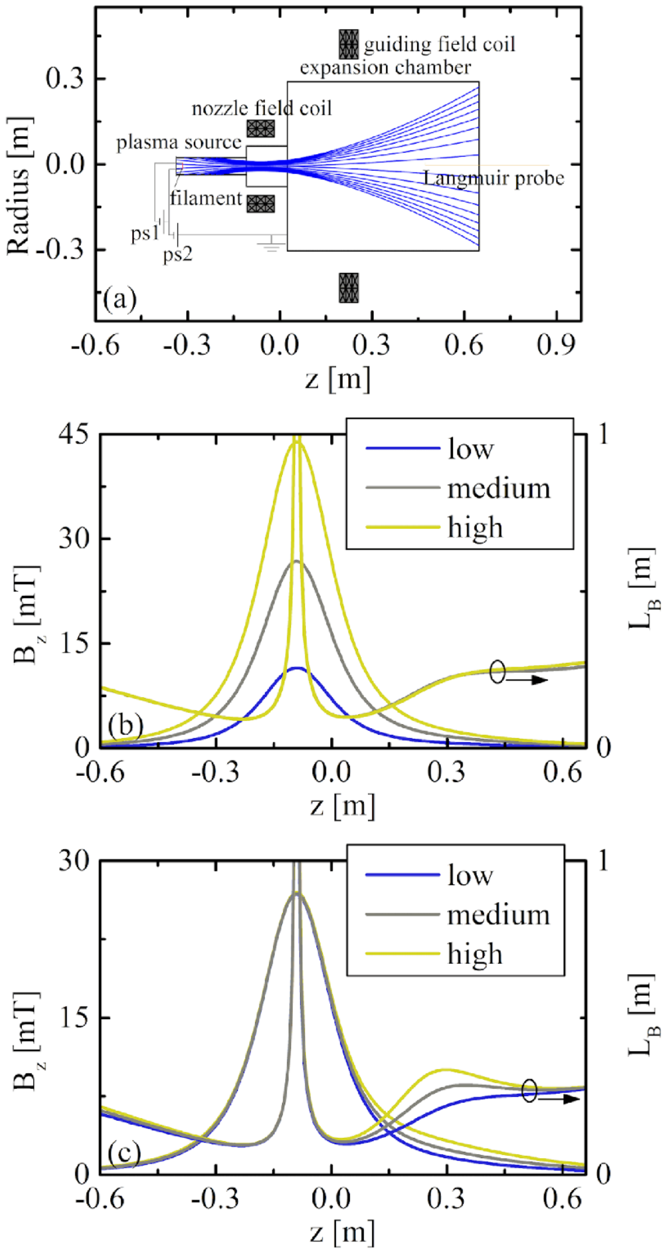

Figure 18. Schematic diagram of the axially symmetric magnetic nozzle shows the filament plasma source and the divergent magnetic field configuration with an axially movable single Langmuir probe. (b) and (c) show magnetic field conditions for strength, B_z, and structure variation $L_B = B_z/\nabla B_z$, respectively. Reproduced from Kim *et al* (2021a).

expansion. This is relevant, in particular, for thrusters such as the AFMPDT and the VASIMR, whose sources generate energetic ions. The parallel ion thermal energy is converted to the directed kinetic energy of the ion gas dynamically (i.e., just as the thermal energy in a conventional gas is converted to directed energy in an expansion to vacuum). The perpendicular ion thermal energy can be converted to parallel energy by the magnetic mirror force on ions, if ions are sufficiently magnetized (which is the situation expected in the VASIMR operation on hydrogen or other light propellants) or by an electrostatic mirror effect, resulting from a radial potential well around the main plume that forms to keep ions with a large perpendicular inside it (Merino and Ahedo 2015, Little and Choueiri 2019). Magnetized ions with an initial swirl at the throat can have

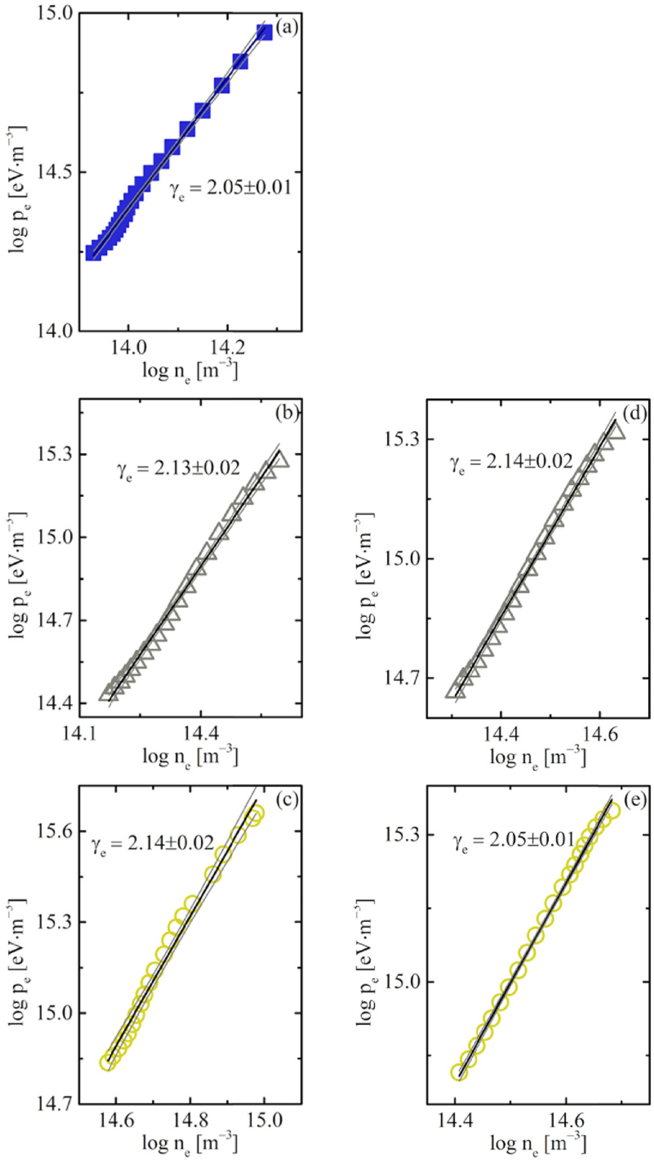

Figure 19. Dependency of the polytropic index, γ_e, on magnetic field strength, B_z; (a) low, (b) medium, and (c) high B_z. The medium B_z condition is assigned a low-gradient scale length, L_B. (d) and (e) are the results of medium and high L_B structure, respectively. The polytropic index is determined by the log–log relationship between the electron pressure, p_e, and the electron density, n_e, averaged over the electron energy probability function. Reproduced from Kim *et al* (2021a).

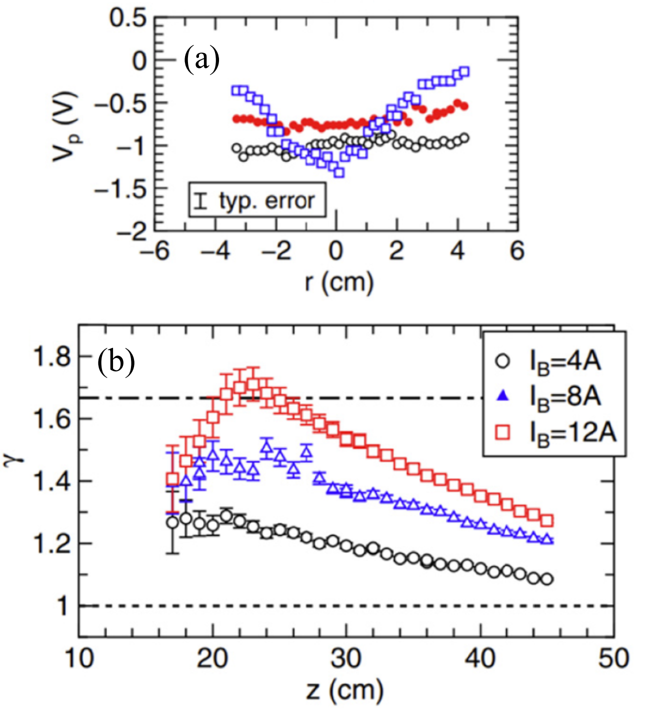

Figure 20. (a) The radial profile of plasma potential, V_p, at the axial location, z, of 20 cm: 4 A (open circle), 7 A (filled circle) and 13 A (open square). (b) Typical axial profiles of the polytropic index, γ, are calculated from the measured electron density and temperature. Reprinted (figure) with permission from Takahashi *et al* (2020a), Copyright (2020) by the American Physical Society.

a diamagnetic azimuthal current that contributes as positive (ion) magnetic thrust.

Far downstream, the plasma must separate from the closed field lines to form a free jet. Otherwise, if the plasma continued attached to the lines, it would return back to the thruster along them, and no momentum would be ejected from the system. Except for huge magnetic strengths and light propellants, ions quickly become effectively unmagnetized downstream. As ions accelerate, their inertial term $m_i u_i^2$ increases, and it was shown that the plasma does not have enough authority to generate the large electric field that would be required to deflect their trajectories to match the magnetic lines (Merino and Ahedo 2014). As a result, ion trajectories become essentially straight and detach from the applied field. As can be observed in figure 24, any form of electron cooling results in smaller electric fields downstream and an earlier separation of the ion flow. Thus, electron thermodynamics are also central to this key issue.

Electrons, on the other hand, can remain magnetized and follow magnetic lines farther downstream: the difference between the ion and electron velocity directions gives rise to a small but nonzero differential current in the meridional plane, even when the plasma jet carries no net current globally (i.e., there is no local current ambipolarity in the plasma). Electron demagnetization remains an open problem in MN theory. However, it is not expected to affect much thrust generation, since electrons are, basically, a confined population.

Another phenomenon that gains importance downstream is the influence of the plasma-induced magnetic field (Merino and Ahedo 2016b). The diamagnetic field tends to open the MN lines, increasing the divergence of the jet, and lower the strength of the net field near the MN axis, facilitating demagnetization. The larger the plasma beta parameter at the throat (i.e., the plasma to magnetic pressure ratio), the earlier in the expansion its effects can be noticed.

Regarding the validation of this model framework, we note that the overall features of the plasma expansion show great agreement with existing experiments, e.g., Takahashi *et al* (2011b), Little *et al* 2014. Detachment predictions from the model explain the observations in Olsen *et al* (2015) and Little

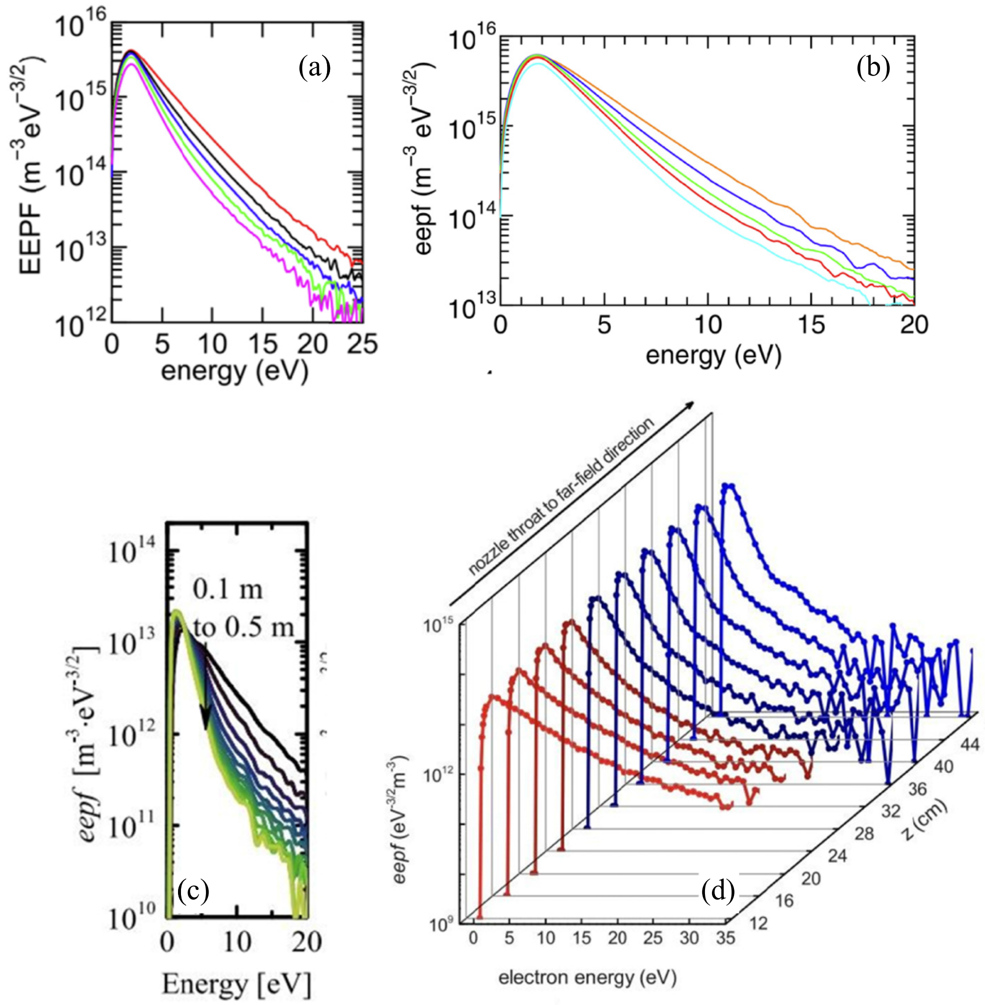

Figure 21. The axial variation of the electron energy probability function (EEPF or *eepf*) on the electron kinetic energy scale. The axial location of (a) 15 (upper most curve) to 40 cm (downer most curve). Reprinted (figure) with permission from Takahashi *et al* (2018), Copyright (2018) by the American Physical Society. (b) 16 (upper most curve) to 36 cm (downer most curve). Reprinted (figure) with permission from Takahashi *et al* (2020a), Copyright (2020) by the American Physical Society. (c) 10 (upper most curve) to 50 cm (downer most curve). Reproduced from Kim *et al* (2021a). © The Author(s). Published by IOP Publishing Ltd. CC BY 4.0, and (d) 12–48 cm from the nozzle throat. Reprinted (figure) with permission from Kim *et al* (2021b), Copyright (2021) by the American Physical Society.

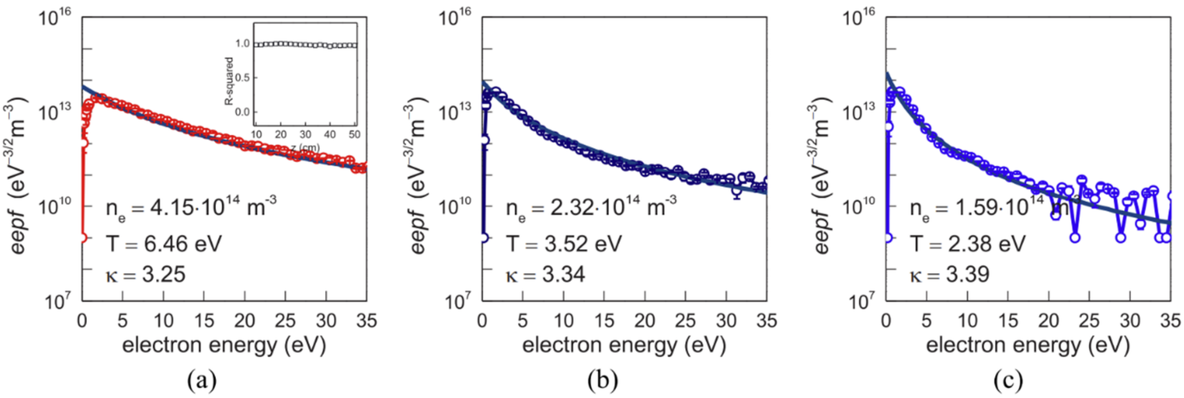

Figure 22. Fitting of the electron energy probability function (*eepf*) by the kappa distribution. The kappa distribution is a function of two independent parameters, temperature, *T*, and kappa, κ. (a) 12 cm, (b) 28 cm, and (c) 48 cm. The inset shows the *R*-squared values (the proportion of the variance of the fitted curve and the experimentally obtained *eepf*s in the range from 3 to 35 eV. Reprinted (figure) with permission from Kim *et al* (2021b), Copyright (2021) by the American Physical Society.

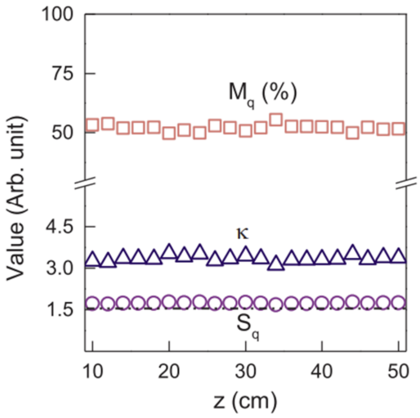

Figure 23. Axial variation of q-metastability M_q, κ, and S_q. Quantifying the entropy enables discussion of the energy flow of the electrons in a MN. The non-extensive entropy S_q in terms of κ is given by $S_q(\kappa) = \kappa - \kappa^{\frac{1}{\frac{2}{3}\kappa+1}}\left[\pi^{-\frac{3}{2}}\left(\kappa-\frac{3}{2}\right)^{\kappa-\frac{1}{2}}\frac{\Gamma(\kappa)}{\Gamma\left(\kappa-\frac{1}{2}\right)}\right]^{\frac{1}{\kappa+\frac{3}{2}}}$. The dashed line indicates the statistical minimum of κ, $3/2$. The kappa obtained along the axial direction is nearly constant at 3.35 ± 0.05. Thermodynamic distance of each stationary state from equilibrium through the q-metastability $M_q = 4\left[(q-1)/(q+1)\right]$, where the equilibrium is described by the classical equilibrium limit $M_q = 0$ for $q \to 1$ and the q-frozen state $M_q = 1$ for $q \to 5/3$, which is the state 100% away from equilibrium. The calculated M_q (expressed as a percentage) for all axial positions is within $52 \pm 0.7\%$, implying invariance of the equilibrium state. Reprinted (figure) with permission from Kim *et al* (2021b), Copyright (2021) by the American Physical Society.

et al (2019). Finally, the diamagnetic induced field generated by the plasma was measured in Roberson *et al* (2011).

3.2. Collisionless electron cooling and kinetic effects

The basic plasma/MN model discussed above assumes certain cooling of the electron population, according to the polytropic law (6). Experimental data, reviewed in section 2, suggests fitting it with a polytropic coefficient $\gamma = 1.2 \pm 0.1$. While this electron model is useful to approximately characterize the plasma beam expansion and the total potential fall in the divergent MN, it does not reveal the physics behind the electron cooling.

The polytropic law (6) indeed provides a closure to the fluid equation hierarchy and, in particular, substitutes the use of the electron energy equation (Ahedo *et al* 2020). Still within a conventional fluid formulation, the energy equation, in the inertialess and stationary case and for an isotropic electron pressure, can be expressed as

$$\nabla \cdot \left[\frac{5}{2}T_e n_e \boldsymbol{u}_e + \boldsymbol{q}_e\right] \simeq \boldsymbol{u}_e \cdot \nabla p_e - Q_{\text{inel}}, \tag{11}$$

where $\boldsymbol{q}_e$ is the heat flux and Q_{inel} represents inelastic losses due to ionization and excitation of atoms. Neglecting Q_{inel} in the near-collisionless limit and postulating an adiabatic behavior (i.e. $\boldsymbol{q}_e = \boldsymbol{0}$), equation (11) is equivalent to

$$\nabla \ln p_e = \gamma \nabla \ln n_e, \tag{12}$$

with $\gamma = 5/3$. If instead, we postulate a 'convective' behavior of the heat flux, expressed by (Ahedo *et al* 2020)

$$\boldsymbol{q}_e = \alpha \frac{5}{2} T_e n_e \boldsymbol{u}_e, \tag{13}$$

with the constant α being the ratio between heat and enthalpy flux, equation (12) continues to be fulfilled but with $\gamma = (5+5\alpha)/(3+5\alpha)$.

For instance, one has $\gamma = 1.2$ for $\alpha = 1.4$. The convective-type law (13) for the heat flux is far different from the conductive Fourier-type law expected in conventional, collisional fluids. This type of law has already been suggested in other weakly-collisional plasmas, such as divertor plasmas in tokamaks (Stangeby *et al* 2010) and laser-produced plasmas (Malone *et al* 1975).

Using equation (13), the energy equation (11) becomes

$$\nabla \cdot \left[\frac{\gamma}{\gamma - 1} T_e n_e \boldsymbol{u}_e\right] \simeq \boldsymbol{u}_e \cdot \nabla p_e - Q_{\text{inel}}, \tag{14}$$

which suggests that the electron fluid behaves as a non-monoatomic adiabatic gas with specific heat ratio γ (Zhou *et al* 2021). We find later that this interpretation agrees well with the different subpopulations of the EVDF. Nonetheless, equation (13) is just a phenomenological law, still not explaining the real physics behind electron cooling. The analysis requires us to acknowledge the near-collisionless character of the electron population, which prevents local thermodynamic equilibrium, thus likely yielding a non-Maxwellian EVDF.

In a weakly collisional framework, the EVDF satisfies the Boltzmann equation (or the Vlasov equation in the collisionless limit) in the six-dimensional phase space $(\boldsymbol{x}, \boldsymbol{v})$. Macroscopic plasma magnitudes are obtained from integral moments of the EVDF, and they satisfy the macroscopic fluid equations, which are also integral moments of the Boltzmann equation. The lack of local thermodynamic equilibrium makes the local solution depend on the global configuration (geometry, magnetic topology, boundary conditions, …) of the problem and is amenable to analytical treatment only in simple configurations.

Martinez-Sanchez *et al* (2015) studied the kinetic expansion of a collisionless, fully magnetized plasma along a paraxial (i.e., quasi-1D) convergent-divergent MN. The paraxial model solves the distribution functions of ions and electrons along the centerline of the MN, considering the variation of the magnetic field strength, which turns out to be equivalent to the variation of the (inverse of the) area of the magnetic streamtube containing the plasma beam. The stationary model considers the distributions of ions and electrons in a far upstream reservoir. Then, exploiting the conservation of the mechanical energy E and the magnetic moment μ, solves for the axial electric field and the distributions at any spatial location. Then, the macroscopic plasma magnitudes are computed from the kinetic solution.

The profile of the electrostatic potential along the paraxial MN, $\phi(z)$, is obtained from the quasi-neutrality condition

$$\int d^3\boldsymbol{v} f_i(z, \boldsymbol{v}) = \int d^3\boldsymbol{v} f_e(z, \boldsymbol{v}), \tag{15}$$

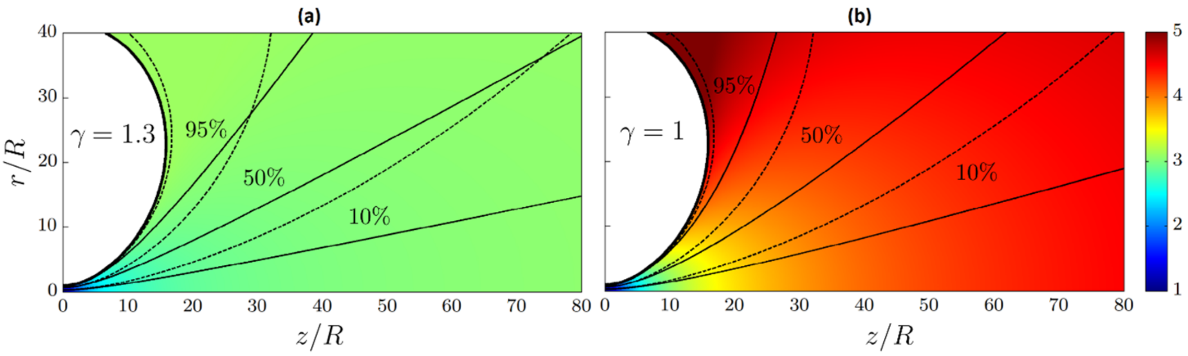

Figure 24. Dimensionless in-plane ion velocity $u_i/\sqrt{m_i/T_{e0}}$ in a magnetic nozzle with polytropic ($\gamma = 1.3$, (a) and isothermal (b) electrons. The ion velocity has been normalized using T_{e0}, the electron temperature at the origin. Dashed lines represent magnetic streamtubes; solid lines are ion streamtubes carrying a given percentage of the total ion flux as indicated. © [2015] IEEE. Reprinted, with permission, from Merino and Ahedo (2015).

which must be solved iteratively, since the ion and electron distributions depend on $\phi(z)$. At each location z, it must be determined which ions and electrons, traveling downstream or upstream, can reach that location. For all upstream EVDFs analyzed so far, $\phi(z)$ is monotonic decreasing from $\phi = 0$ upstream to $\phi = \phi_\infty (< 0)$ downstream, which facilitates the determination of $\phi(z)$. Finally, assuming a current-free plasma beam, the total potential fall $|\phi_\infty|$ in the MN is self-adjusted in the same way that the potential fall is adjusted in a non-neutral Debye sheath in front of a dielectric wall: the value of $|\phi_\infty|$ does not change the net ion current but it very effectively controls the net electron current, so $|\phi_\infty|$ self-adjusts to satisfy the current-free condition. This explains that $|e\phi_\infty|$ depends very much on the properties of the EVDF, and typically it amounts to several times the upstream electron temperature. Sample solutions of the electrostatic potential profile ϕ in a current-free MN and two current-carrying MNs are shown in figure 25 versus $B(z)$.

In the paraxial convergent–divergent MN, the axial motion of an individual ion or electron with energy E and magnetic moment μ is determined by the electrostatic and the magnetic mirror forces, according to

$$\frac{1}{2} m_\alpha v_z^2 = E - \mu B(z) - Z_\alpha e\phi(z), \tag{16}$$

where $\alpha = i, e$, and $Z_\alpha = \pm 1$ is the charge number of the species. The electrostatic field accelerates ions and decelerates electrons axially in the convergent and divergent MN regions. On the other hand, the magnetic mirror decelerates both ions and electrons on the convergent part and accelerates them axially on the divergent one. Combining the electrostatic and magnetic mirror effects, the following situations take place: upstream ions with high μ and low E are reflected back to the reservoir within the convergent region, while any ion reaching the MN throat is accelerated downstream (explaining that $|\phi_\infty|$ has no control on the ion current). Therefore, the population of ions in the reservoir is divided into *free* and *reflected* subpopulations, and all ions in the divergent region are free.

Regarding electrons from the reservoir, similar subpopulations exist, but only a narrow interval of high E and low μ

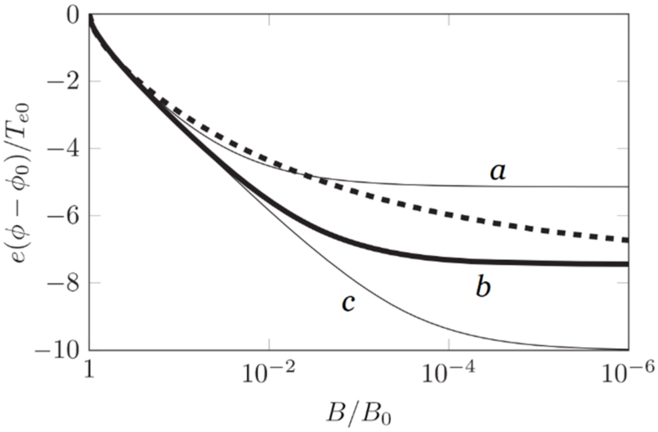

Figure 25. Dimensionless electrostatic potential $e(\phi - \phi_0)/T_{e0}$ (normalized with T_{e0}, the electron temperature at the throat) along the axis of a divergent MN, plotted against the relative magnetic field strength B/B_0. Xe as propellant. The solid lines represent kinetic simulations with a net current $j/(en_{e0}\sqrt{T_{e0}/m_i}) = -7$ (a), 0 (b), and $+0.9$ (c). The dotted line represents a polytropic model that results in the same potential fall far downstream as the globally current-free kinetic result (thick line b). Reproduced from Merino *et al* (2021). © The Author(s). Published by IOP Publishing Ltd. CC BY 4.0.

constitute the *free* electron subpopulation, even on the divergent region. The main novelty is the existence of a third subpopulation of *doubly trapped* electrons. These are electrons that bounce back-and-forth axially between two locations on the divergent MN region (Martinez-Sanchez *et al* 2015). In their downward trip, they are accelerated by the magnetic mirror and decelerated by the electric field and vice versa in their upstream trip. Since the trajectories of these electrons are disconnected from the upstream reservoir, their distribution cannot be determined by the stationary model. Different postulates on this population lead to different expansion gradients and collective electron cooling (Ramos *et al* 2018). Figure 26 illustrates the EVDF and its different subdomains in the convergent and the divergent part of a MN, when the doubly trapped electron region (DTER) in the divergent part is assumed to have the same distribution as the rest of the electrons.

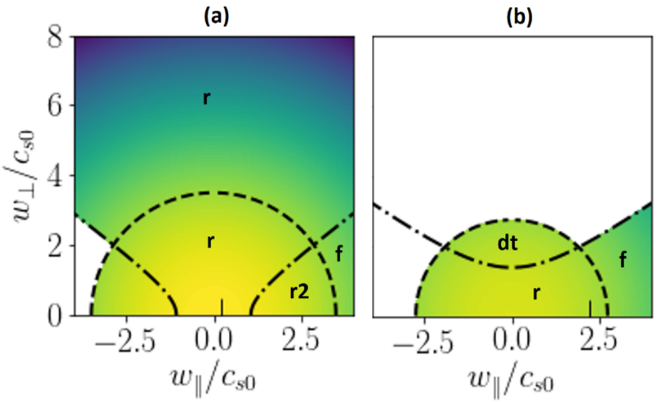

Figure 26. Electron velocity distribution function (EVDF) on the convergent side (a) and divergent side (b) of a MN. Regions of reflected I, doubly trapped (dt) and free (f) electrons are indicated. On the convergent side, reflected electrons that trespass into the divergent side are indicated as (r2). Limiting lines refer to the value of the effective potential in the axial motion of electrons at the throat (dash-dot line) and at infinity downstream (dashed line). Figure adapted from (Ahedo *et al* 2020) with permissions; refer to that work for a detailed discussion of this kinetic simulation of the EVDF. Reproduced from Ahedo *et al* (2020).

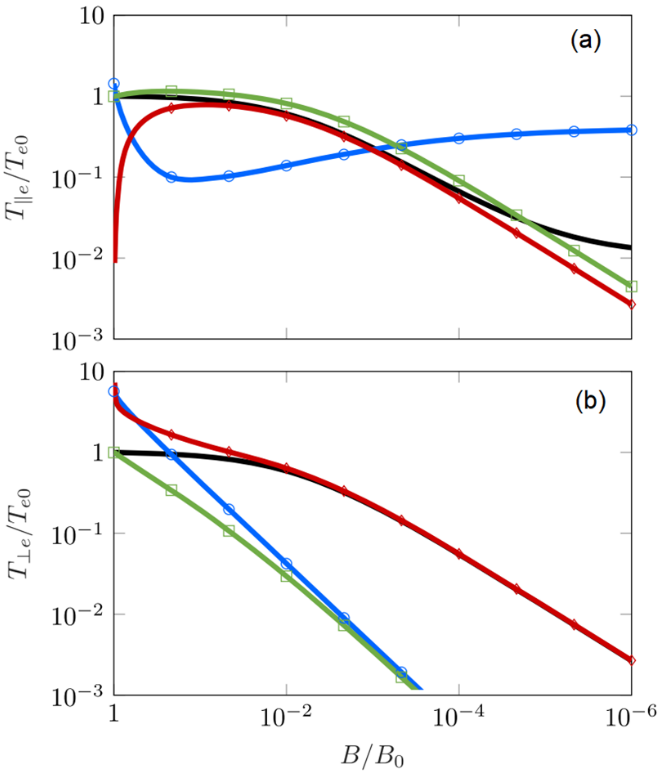

Figure 27. Parallel (a) and perpendicular (b) temperatures of representative free (blue circles), reflected (green squares), doubly trapped (red diamonds) electrons in a divergent MN, under the assumption that the doubly trapped regions of the EVDF have the same distribution as the rest of the electrons. Reproduced from Merino *et al* (2021).

In a collisionless plasma, temperatures are just a measure of the velocity dispersion of each species and generally they are not settled locally. Assuming upstream Maxwellian distributions of ions and electrons, both temperature anisotropy and the cooling of ions and electrons develop along the convergent-divergent MN. Temperature anisotropy is mainly related to magnetic mirror effects. This is well known on a single particle, but collective magnetic mirror effects are subtler (Ahedo *et al* 2020). For instance, on the MN convergent side, the ratio $T_{\perp i}/T_{\parallel i}$, between ion perpendicular and parallel temperatures increases much, but $T_{\perp e}/T_{\parallel e}$ remains close to 1, and thus f_e remains close to Maxwellian, so the collective magnetic mirror 'force' is strong on ions and near null on electrons on that MN part. On the other hand, on the MN divergent side, the magnetic mirror causes both $T_{\perp i}/T_{\parallel i}$ and $T_{\perp e}/T_{\parallel e}$ to decrease and tend to zero. The behavior of the temperature of each electron subspecies is shown in figure 27. These disparities indicate that the combined effects of the magnetic mirror and the electric field redistributes the ions and electrons very differently within the EVDF's $\boldsymbol{v}$-phase-space. Electron cooling on the MN divergent side is mainly the consequence of the shrinking of the EVDF's $\boldsymbol{v}$-phase-space attainable by electrons, as shown in (Martínez-Sánchez *et al* 2015, Ahedo *et al* 2020) and in figure 26. Comparison of these results with the experimental measurements reviewed in section 2 reveals an overall agreement in terms of electron cooling trends.

In a divergent MN, all ions are free and constitute a single population that becomes hypersonic downstream, so the particularities of the ion temperatures are not very relevant; there are still some differences in the physical response if upstream ions are hot or cold (Martinez-Sanchez *et al* 2015, Ahedo *et al* 2020). The situation is very different for electrons, which are constituted by a mixture of the three subpopulations, which have different properties. Doubly trapped electrons are nearly isotropic, but free and reflected subpopulations are anisotropic; also, free electrons are hotter downstream than the two confined subpopulations. The properties of the resulting electron mixture come from weighing the properties of the three subpopulations with their partial densities. This explains why simple physical laws (e.g., in the form of a polytropic equation) are elusive for electron mixtures and highlight the importance of determining correctly the number of doubly-trapped electrons and their distribution. The theory of (Martinez-Sanchez *et al* 2015) and (Ahedo *et al* 2020) postulated that the phase region of doubly-trapped electrons was fully populated.

There are at least three mechanisms giving access to the DTER, enabling filling it (partially) up. One is during the transient formation of the MN, a second one is due to occasional collisional events that bring electrons into that region, and a third one is electron-related instabilities. The first one alone leads to a transient-dependent stationary solution, whereas any presence of the latter two mechanisms would relax the solution slowly toward a single steady-state one. Sanchez-Arriaga *et al* (2018) developed a time-dependent, direct-Vlasov code for the paraxial MN to assess the transient problem. Contrary to the stationary model relying only on integral equations, the Poisson's equation needs to be solved and the MN domain for numerical integration is finite, which poses some difficulties

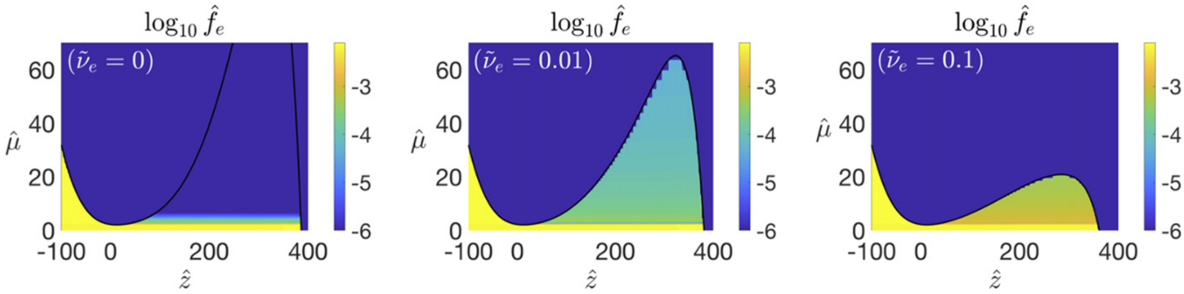

Figure 28. Dimensionless EVDF $\hat{f}_e(\hat{\mu}, \hat{E})$ in a particular MN as the collision frequency is increased, obtained with the code of (Zhou *et al* 2021). The EVDF is presented as a function of the normalized magnetic moment $\hat{\mu} = \mu B_0/T_{e0}$ and energy $\hat{E} = E/T_{e0}$. These plots correspond with energy $\hat{E} = 2.85$. The black line delimits the allowed region from the forbidden region in this phase space. Reproduced from Zhou *et al* (2021).

for downstream boundary conditions. We find a relatively low fill-up fraction of the DTER compared to the full DTER postulated in (Martinez-Sanchez *et al* 2015, Ahedo *et al* 2020). This difference has practically no implications on the total potential fall, but it does have it on the expansion plasma profiles and the level of electron cooling (since, as explained above, the electron temperatures are weighted averages over the three subpopulations).

Zhou *et al* (2021) extended the model of Sanchez-Arriaga *et al* (2018) to the weak-collisional regime using a BGK approach, which affects almost exclusively trapped particles. It is demonstrated that the filling level of the DTER increases with the effective electron collision frequency but, as long as collisions are scarce compared to the typical electron bouncing time in the DTER, there is no complete filling, since electrons can flow in and out of that region until an equilibrium is reached [figure 28]. In this weakly collisional regime, collisions tend to decrease the temperature anisotropy and the electron cooling is more moderate, which is more in line with experimental data. Importantly, collisions erase the transient history of the MN formation, making the stationary solution unique. It must be noted that reaching a stationary state is rather costly computationally in the weak-collisional regime, as the characteristic time of convergence towards this solution scales inversely with the collision frequency.

Once the basic physics of electron temperature anisotropy and cooling has been established, the question of whether a reliable macroscopic electron (and ion) model for the MN weak-collisionality scenario can be derived, and remain usable within the fluid formalism, remains open. For the paraxial MN model and no collisions between two particles of different species, the kinetic solution for species $j = i, e$, satisfies the following macroscopic equations,

$$\frac{n_j u_j}{B} = \text{const}, \tag{17}$$

$$m_j n_j u_j \frac{\mathrm{d}u_j}{\mathrm{d}z} + Z_j e \frac{\mathrm{d}\phi}{\mathrm{d}z} + \frac{\mathrm{d}\left(n_j T_{\parallel j}\right)}{\mathrm{d}z} + n_j \left(T_{\perp j} - T_{\parallel j}\right) \frac{\mathrm{d}\ln B}{\mathrm{d}z} = 0, \tag{18}$$

$$\left(Z_j e\phi + \frac{1}{2} m_j u_j^2 + h_j\right) \frac{n_j u_j}{B} + \frac{q_j}{B} = \text{const}, \tag{19}$$

$$\frac{T_{\perp j} n_j u_j + q_{\perp j}}{B^2} = C_j. \tag{20}$$

Here, u_j is the macroscopic velocity parallel to the magnetic line, Z_j is the species charge number, $h_j = 3T_{\parallel j}/2 + T_{\perp j}$ is the enthalpy per particle, $q_j = (m_j/2)\int d^3\boldsymbol{v} f_e c_{jz} c_j^2, \boldsymbol{c}_j = \boldsymbol{v} - u_j \mathbf{1}_z$, is the heat flux parallel to the magnetic line, $q_{\perp j} = (m_j/2)\int d^3\boldsymbol{v} f_e c_{jz} c_{\perp j}^2$ is the heat flux parallel to the magnetic line *of perpendicular energy*, and C_j a function dependent on intraspecies collisions (it is constant in the collisionless limit).

Equation (17) expresses the conservation of the species flow, with $1/B$ being proportional to the area of the plasma beam. The momentum equation (18)—along the magnetic lines—illustrates that a collective magnetic mirror effect is intimately linked to the development of temperature anisotropy. Equation (19) expresses the conservation of total energy, with $Z_j e\phi$ and $h_j + q_j/(n_j u_j)$ the potential and thermal energy per particle, respectively. Equation (20) sets the conservation of perpendicular energy. Its simple form is because it refers only to the MN centerline where there are no perpendicular gradients. The dependence on $1/B^2$ explains that the perpendicular thermal energy flux $T_{\perp j} n_j u_j + q_{\perp j}$ goes to zero as $B \to 0$.

The closure of the set of equations (17)–(20) requires defining laws for the heat fluxes q_j and $q_{\perp j}$, in terms of low-order magnitudes (n_j, u_j, $T_{\parallel j}, T_{\perp j}$) and independent of fourth-order integral moments. For collisional species, $q_{\perp j} = 2q_j/3$, and q_j satisfies the conductive Fourier law. For weakly collisional species, simple laws do not exist in general, so the best that can be expected are approximate laws for particular regions of the discharge. Centering the attention on the electrons and the expansion in the divergent MN, Ahedo *et al* (2020) and Zhou *et al* (2021) showed that $q_{\perp e}$ can be neglected, and q_e does not follow a conductive (i.e., Fourier) law $q_e \propto \mathrm{d}T_e/\mathrm{d}z$. Instead, the convective-type law (13) offers an acceptable approximation.

In the context of tokamaks and plasma-laser applications and in order to cover intermediate collisional regimes, Bell *et al* (1985), Zawaideh *et al* (1988) and Stangeby *et al* (2010) proposed hybrid closure laws for the heat flux with one fitting parameter. Following this approach Zhou *et al* (2021) has attempted to fit the heat flux in a divergent MN nozzle with a two-parameter hybrid law

$$\boldsymbol{q}_e = \alpha T_e n_e \boldsymbol{u}_e - \beta K \nabla T_e, \tag{21}$$

with K the thermal conductivity, and α and β two fitting parameters that depend on the electron collisionality. The kinetic results demonstrate that, in the evolution from a collisionless scenario to a collisional one, α goes from $O(1)$ to 0 and β from 0 to 1, which supports the reliability of this hybrid approach.

The kinetic studies commented on so far are limited to the paraxial, fully magnetized MN model. Merino *et al* (2021) have recently extended the fully magnetized case to a 2D configuration, where the response in each magnetic line can still be tackled independently. Anisotropy, cooling, and parallel heat flux follow exactly the same trends, while plasma parameters adapt to radially varying boundary conditions.

Partial magnetization of ions leads to a more complex 2D problem, still unresolved for kinetic electrons, but no fundamental changes are expected in the electron response. However, freeing the postulate of full-magnetization of electrons, which certainly happens in any real MN sufficiently far downstream, can imply important changes. The effect of this gradual demagnetization on $T_{\|e}$ and $T_{\perp e}$ is pending analysis. Nonetheless, studies by Merino *et al* (2018) on an unmagnetized, collisionless, paraxial, plasma plume, with electrons under electrostatic confinement only, show a collective behavior very similar to the one in the MN in terms of anisotropy and cooling of the electron temperature, at least around the plume axis. Instead of performing gyro-orbits around magnetic lines, electrons perform large excursions in a radial electrostatic potential well, and this brings about an 'electrostatic mirror' effect that plays an analogous similar role to the magnetic mirror effect.

We conclude this section by discussing the effects of electron thermodynamics on the performance of the plasma thruster, which results from the combined effect of the MN and the plasma source. In the near-collisionless MN, the power of the plasma beam remains constant along the nozzle, and we observe only a transfer of energy from electrons to ions and the radial divergence of the beam. As Zhou *et al* (2022) showed, a higher electron cooling implies that the beam expansion in the MN takes place at a shorter distance and the electron temperature at the MN throat is larger; both effects help to increase the thrust efficiency. Thus, higher electron cooling implies that the average T_e in the source is larger too. This causes both wall-loss and beam-power densities (i.e., per electron) to be higher, while the trend of the ionization and excitation losses depends on the particular source configuration. If we consider a given deposition power P_a and assume that inelastic losses are essentially unaffected, a higher T_e implies a lower average plasma density in the source. In terms of thrust efficiency, Zhou *et al* (2022) found that the MN electron cooling barely affects the contribution of the source to thrust efficiency. Adding the MN and source behavior, we conclude that a faster electron cooling favors slightly the thrust efficiency. Current modeling and experimental understanding suggest that the central reasons for the low efficiency of current electrodeless plasma thrusters are likely a combination of poor power coupling efficiency from the circuit to the plasma and large plasma and power losses to the walls inside the source (Ahedo 2011a, Sánchez-Villar *et al* 2023).

4. Conclusions and future challenges

In this review, we discuss the fundamental physics of the kinetics of electron cooling in MNs and magnetically expanding plasmas. When considering actual plasma devices using a power source, a non-local coupling of RF or MW power with electrons often occurs, e.g., via a wave-heating mode; adiabatic conditions cannot be maintained. The investigation of the polytropic index under the experiments having a heat source and loss would also contribute to understand the energy transfer process by combining with the detailed physical process, thus, well-controlled experiments will be required to investigate such a process in laboratories.

On the theoretical side, it has been argued that, while fluid models enable a sufficient description of certain MN physical mechanisms, there are currently no self-consistent closure laws for the non-local electron thermodynamics in quasi-collisionless regimes. The most commonly used closure is an isotropic, polytropic law, with an empirical exponent γ fitted to the observed electron cooling to experimental results. Since the electric fields that accelerate ions in the MN are proportional to the local value of the electron temperature, obtaining a correct description of electron cooling and anisotropy is essential for the correct prediction of MN performance figures and ion detachment downstream.

A paraxial kinetic model of electrons has been reviewed, which enables the self-consistent solution of the EVDF and electrostatic potential, and therefore the self-consistent solution of electron cooling and anisotropy development. Electrons are seen to divide into free, reflected, and doubly trapped electrons depending on their location along the MN, their energy, and their magnetic moment. The distribution of doubly-trapped electrons cannot be assessed from the steady-state, collisionless description of the problem, and requires tackling the transient and/or including the effect of small collisionality in the MN. The total potential fall along the plume is intimately linked to the number of free electrons and the net electron current in the device. Each electron subpopulation cools down differently along the expansion and an initially isotropic EVDF becomes anisotropic downstream. While one can define a polytropic model that results in the same total potential fall as the globally current-free kinetic model, the map of the electrostatic potential differs substantially, and the anisotropy is missed.

More advanced closure laws may need to resort to modeling the electron heat fluxes in such a way that they respect the kinetic solution of the plasma expansion. Other open challenges in modeling include the self-consistent simulation of 2D MNs and the study of electron demagnetization and detachment. Given the large computational cost of direct kinetic simulation, smart approaches, such as hybrid combinations of fluid and kinetic descriptions to lower the number of numerical operations, may offer a way forward in this area.

Data availability statement

The data that support the findings of this study are available from the corresponding authors upon reasonable request.

Acknowledgments

June Young Kim's work was supported by the National Research Foundation of Korea (NRF) grant funded by the Korea Government (MSIT) (RS-2023-00208968).

Kazunori Takahashi's work was supported by Grant-in-Aid for Scientific Research (Grant No. 23H05442) from the Japan Society for the Promotion of Science and Fusion Oriented REsearch for disruptive Science and Technology (FOREST) from Japan Science and Technology Agency (Grant No. JPMJFR212A).

Mario Merino's work was supported by the European Research Council (ERC) under the European Union's Horizon 2020 research and innovation programme (Project ERC Starting Grant ZARATHUSTRA, Grant Agreement No. 950466).

Eduardo Ahedo's work is part of the ESPEOS R+D+i Project PID2019-108034RB-I00, funded by MCIN/AEI/10.13039/501100011033/.

Author contributions

June Young Kim: Supervision (lead); Formal analysis (lead); Investigation (lead); Writing—original draft (lead); Writing—review & editing (lead). Kyoung-Jae Chung: Formal analysis (supporting); Writing—review & editing (supporting). Kazunori Takahashi: Validation (supporting); Writing—original (supporting); Writing—review & editing (supporting). Mario Merino: Investigation (equal); Writing—original draft (equal); Writing—review & editing (equal). Eduardo Ahedo: Investigation (supporting); Writing—original draft (equal); Writing—review & editing (supporting).

Conflict of interest

The authors have no conflicts to disclose.

ORCID iDs

June Young Kim https://orcid.org/0000-0001-6529-3607
Kyoung-Jae Chung https://orcid.org/0000-0003-3139-2433
Kazunori Takahashi https://orcid.org/0000-0001-5690-1893
Mario Merino https://orcid.org/0000-0001-7649-3663
Eduardo Ahedo https://orcid.org/0000-0003-2148-4553

References

Agnihotri A N, Kelkar A H, Kasthurirangan S, Thulasiram K V, Desai C A, Fernandez W A and Tribedi L C 2011 An ECR ion source-based low-energy ion accelerator: development and performance *Phys. Scr.* **2011** 014038

Ahedo E 2011a Plasmas for space propulsion *Plasma Phys. Control. Fusion* **53** 124037

Ahedo E 2011b Double-layer formation and propulsive assessment for a three-species plasma expanding in a magnetic nozzle *Phys. Plasmas* **18** 033510

Ahedo E, Correyero S, Navarro-Cavallé J and Merino M 2020 Macroscopic and parametric study of a kinetic. plasma expansion in a paraxial magnetic nozzle *Plasma Sources Sci. Technol.* **29** 045017

Ahedo E and Martínez Sánchez M 2009 Theory of a stationary current-free double layer in a collisionless plasma *Phys. Rev. Lett.* **103** 135002

Ahedo E and Merino M 2010 Two-dimensional supersonic plasma acceleration in a magnetic nozzle *Phys. Plasmas* **17** 073501

Ahedo E and Merino M 2011 On plasma detachment in propulsive magnetic nozzles *Phys. Plasmas* **18** 053504

Ahedo E and Merino M 2012 Two-dimensional plasma expansion in a magnetic nozzle: separation due to. electron inertia *Phys. Plasmas* **19** 083501

Andersen S A, Jensen V O, Nielsen P and D'Angelo N 1969 Continuous supersonic plasma wind tunnel *Phys. Fluids* **12** 557–60

Andrenucci M 2010 Magnetoplasmadynamic thrusters *Encyclopedia of Aerospace Engineering*

Andrews S, Di Fede S and Magarotto M 2022 Fully kinetic model of plasma expansion in a magnetic nozzle *Plasma Sources Sci. Technol.* **31** 035022

Arefiev A V and Breizman B N 2004 Theoretical components of the VASIMR plasma propulsion concept *Phys. Plasmas* **11** 2942–9

Arefiev A V and Breizman B N 2005 Magnetohydrodynamic scenario of plasma detachment in a magnetic nozzle *Phys. Plasmas* **12** 043504

Arefiev A V and Breizman B N 2008 Ambipolar acceleration of ions in a magnetic nozzle *Phys. Plasmas* **15** 042109

Bell A R 1985b Non-Spitzer heat flow in a steadily ablating laser-produced plasma *Phys. Fluids* **28** 2007

Boni F, Jarrige J and Désangles V 2022 Plasma expansion and electron properties in a magnetic nozzle. Electrode-less thruster *Int. Electric Propulsion Conf.*

Boswell R W, Takahashi K, Charles C and Kaganovich I D 2015 Non-local electron energy probability function in a plasma expanding along a magnetic nozzle *Front. Phys.* **3** 14

Boyd I D and Ketsdever A 2001 Interactions between spacecraft and thruster plumes *J. Spacecr. Rockets* **38** 380

Breizman B N, Tushentsov M R and Arefiev A V 2008 Magnetic nozzle and plasma detachment model for a steady-state flow *Phys. Plasmas* **15** 057103

Capitelli M, Casavola A, Colonna G and De Giacomo A 2004 Laser-induced plasma expansion: theoretical and experimental aspects *Spectrochim. Acta* B **59** 3

Chang-Diaz F 2000b The VASIMR rocket *Sci. Am.* **283** 90–97

Chang-Diaz F, Squire J, Bengtson R, Breizman B, Carter M and Baity F 2000a The physics and engineering of the VASIMR engine *36th AIAA/ASME/SAE/ASEE Joint Propulsion Conf. and Exhibit* p 3756

Charles C 2010 High density conics in a magnetically expanding helicon plasma *Appl. Phys. Lett.* **96** 051502

Charles C, Boswell R W, Cox W, Laine R and MacLellan P 2008 Magnetic steering of a helicon double layer thruster *Appl. Phys. Lett.* **93** 201501

Choueiri E 1998 Scaling of thrust in self-field magnetoplasmadynamic thrusters *J. Propuls. Power* **14** 744–53

Conrads H and Schmidt M 2000 Plasma generation and plasma sources *Plasma Sources Sci. Technol.* **9** 44
Correyero S, Jarrige J, Packan D and Ahedo E 2019 Plasma beam characterization along the magnetic nozzle of an ECR thruster' *Plasma Sources Sci. Technol.* **28** 095004
Deline C A, Bengtson R D, Breizman B N, Tushentsov M R, Jones J E, Chavers D G, Dobson C C and Schuettpelz B M 2009 Plume detachment from a magnetic nozzle *Phys. Plasmas* **16** 033502
Denavit J 1979 Collisionless plasma expansion into a vacuum *Phys. Fluids* **22** 1384
Drake R P and Drake R P 2006 *Introduction to High-Energy-Density Physics* (Berlin: Springer)
Ebersohn F, Girimaji S, Staack D, Shebalin J, Longmier B and Olsen C 2012 Magnetic nozzle plasma plume: review of crucial physical phenomena *48th AIAA/ASME/SAE/ASEE Joint Propulsion Conf. & Exhibit* p 4274
Fruchtman A, Takahashi K, Charles C and Boswell R W 2012 A magnetic nozzle calculation of the force on a plasma *Phys. Plasmas* **19** 033507
Ghosh S, Yadav S, Barada K K, Chattopadhyay P K, Ghosh J, Pal R and Bora D 2017 Formation of annular plasma downstream by magnetic aperture in the helicon experimental device *Phys. Plasmas* **24** 020703
Gopal A *et al* 2013 Observation of gigawatt-class THz pulses from a compact laser-driven particle accelerator *Phys. Rev. Lett.* **111** 074802
Gulbrandsen N and Fredriksen Å 2017 RFEA measurements of high-energy electrons in a helicon plasma device with expanding magnetic field *Front. Phys.* **5** 2
Hepner S T and Jorns B 2021 Anomalous electron thermal conductivity in a magnetic nozzle *AIAA Propulsion. and Energy 2021 Forum* p 3399
Hepner S, Wachs B and Jorns B 2020 Wave-driven non-classical electron transport in a low temperature magnetically expanding plasma *Appl. Phys. Lett.* **116** 263502
Hooper E B 1993 Plasma detachment from a magnetic nozzle *J. Propuls. Power* **9** 757–63
Hu Y, Huang Z, Cao Y and Sun Q 2021 Kinetic insights into thrust generation and electron transport in a magnetic nozzle *Plasma Sources Sci. Technol.* **30** 075006
Hu Y and Wang J 2015 Electron properties in collisionless mesothermal plasma expansion: fully kinetic simulations *IEEE Trans. Plasma Sci.* **43** 2832–8
Imai R and Takahashi K 2021 Demonstrating a magnetic steering of the thrust imparted by the magnetic nozzle radiofrequency plasma thruster *Appl. Phys. Lett.* **118** 264102
Kaganovich I D *et al* 2020 Physics of E $\times$ B discharges relevant to plasma propulsion and similar technologies *Phys. Plasmas* **27** 120601
Kim J Y, Chung K S, Kim S, Ryu J H, Chung K-J and Hwang Y S 2018 Thermodynamics of a magnetically expanding plasma with isothermally behaving confined electrons *New J. Phys.* **20** 063033
Kim J Y, Go G, Hwang Y S and Chung K-J 2021a Dependence of the polytropic index of plasma on magnetic field *New J. Phys.* **23** 052001
Kim J Y, Jang J Y, Choi J, Wang J-I, Jeong W I, Elgarhy M A I, Go G, Chung K-J and Hwang Y S 2021c Magnetic confinement and instability in partially magnetized plasma *Plasma Sources Sci. Technol.* **30** 025011
Kim J Y, Jang J Y, Chung K S, Chung K-J and Hwang Y S 2019 Time-dependent kinetic analysis of trapped electrons in a magnetically expanding plasma *Plasma Sources Sci. Technol.* **28** 07LT01
Kim J Y, Lee H-C, Go G, Choi Y H, Hwang Y S and Chung K-J 2021b Exploring the nonextensive thermodynamics of partially ionized gas in magnetic field *Phys. Rev.* E **104** 045202
Kodys A and Choueiri E 2005 A critical review of the state-of-the-art in the performance of applied-field magnetoplasmadynamic thrusters *41st AIAA/ASME/SAE/ASEE Joint Propulsion Conf. & Exhibit* p 4247
Kuriki K and Okada O 1970 Experimental study of a plasma flow in a magnetic nozzle *Phys. Fluids* **13** 2262–9
Lafleur T, Cannat F, Jarrige J, Elias P Q and Packan D 2015 Electron dynamics and ion acceleration in expanding-plasma thrusters *Plasma Sources Sci. Technol.* **24** 065013
Levchenko I, Xu S, Mazouffre S, Lev D, Pedrini D, Goebel D, Garrigues L, Taccogna F and Bazaka K 2020 Perspectives, frontiers, and new horizons for plasma-based space electric propulsion *Phys. Plasmas* **27** 020601
Li M, Merino M, Ahedo E and Tang H 2019 On electron boundary conditions in PIC plasma thruster plume simulations *Plasma Sources Sci. Technol.* **28** 034004
Little J M and Choueiri E Y 2013 Thrust and efficiency model for electron-driven magnetic nozzle *Phys. Plasmas* **20** 103501
Little J M and Choueiri E Y 2014 Critical condition for plasma confinement in the source of a magnetic nozzle flow *IEEE Trans. Plasma Sci.* **43** 277–86
Little J M and Choueiri E Y 2016 Electron cooling in a magnetically expanding plasma *Phys. Rev. Lett.* **117** 225003
Little J M and Choueiri E Y 2019 Electron demagnetization in a magnetically expanding plasma *Phys. Rev. Lett.* **123** 145001
Litvinov I I 1971 Stationary efflux into a vacuum by a dual-temperature fully ionized plasma *J. Appl. Mech. Tech. Phys.* **12** 793–802
Longmier B W *et al* 2011 Ambipolar ion acceleration in an expanding magnetic nozzle *Plasma Sources Sci. Technol.* **20** 015007
Malone R C, McCrory R L and Morse R L 1975 Indications of strongly flux-limited electron thermal conduction in laser-target experiments *Phys. Rev. Lett.* **34** 12
Martinez-Sanchez M, Navarro-Cavallé J and Ahedo E 2015 Electron cooling and finite potential drop in a magnetized plasma expansion *Phys. Plasmas* **22** 053501
Merino M and Ahedo E 2013 Two-dimensional quasi-double-layers in two-electron-temperature, current-free plasmas *Phys. Plasmas* **20** 023502
Merino M and Ahedo E 2014 Plasma detachment in a propulsive magnetic nozzle via ion. demagnetization *Plasma Sources Sci. Technol.* **23** 032001
Merino M and Ahedo E 2015 Influence of electron and ion thermodynamics on the magnetic nozzle plasma expansion *IEEE Trans. Plasma Sci.* **43** 244–51
Merino M and Ahedo E 2016a Magnetic nozzles for space plasma thrusters (https://doi.org/10.1081/E-EPLT-120053936)
Merino M and Ahedo E 2016b Effect of the plasma-induced magnetic field on a magnetic nozzle *Plasma Sources Sci. Technol.* **25** 045012
Merino M and Ahedo E 2017 Contactless steering of a plasma jet with a 3D magnetic nozzle *Plasma Sources Sci. Technol.* **26** 095001
Merino M, Mauriño J and Ahedo E 2018 Kinetic electron model for plasma thruster plumes *Plasma Sources Sci. Technol.* **27** 035013
Merino M, Nuez J and Ahedo E 2021 Fluid-kinetic model of a propulsive magnetic nozzle *Plasma Sources Sci. Technol.* **30** 115006
Mora P 2003 Plasma expansion into a vacuum *Phys. Rev. Lett.* **90** 185002
Olsen C S *et al* 2015 Investigation of plasma detachment from a magnetic nozzle in the plume of the VX-200 magnetoplasma thruster *IEEE Trans. Plasma Sci.* **43** 252–68
Plihon N, Chabert P and Corr C S 2007 Experimental investigation of double layers in expanding plasmas *Phys. Plasmas* **14** 013506

Raadu M A 1979 Expansion of a plasma injected from an electrodeless gun along a magnetic field *Plasma Phys.* **21** 331
Ramos J J, Merino M and Ahedo E 2018 Three dimensional fluid-kinetic model of a magnetically guided plasma jet *Phys. Plasmas* **25** 061206
Roberson B, Winglee R and Prager J 2011 Enhanced diamagnetic perturbations and electric currents observed downstream of the high power helicon *Phys. Plasmas* **18**
Samir U, Wright K H Jr and Stone N H 1983 The expansion of a plasma into a vacuum: basic phenomena and processes and applications to space plasma physics *Rev. Geophys.* **21** 7
Sánchez-Arriaga G, Zhou J, Ahedo E, Martínez-Sánchez M and Ramos J J 2018 Kinetic features and non-stationary electron trapping in paraxial magnetic nozzles *Plasma Sources Sci. Technol.* **27** 035002
Sanchez-Villar Á, Boni F, Désangles V, Jarrige J, Packan D, Ahedo E and Merino M 2023 Comparison of a hybrid model and experimental measurements for a dielectric-coated coaxial ECR thruster *Plasma Sources Sci. Technol.* **32** 014002
Sercel J C 1987 Electron-cyclotron-resonance (ECR) plasma acceleration *19th AIAA, Fluid Dynamics, Plasma. Dynamics, and Lasers Conf.* p 1407
Sercel J C 1990 A simple model of plasma acceleration in a magnetic nozzle *21st AIAA Int. Electric Propulsion Conf.* AIAA-90-2597
Sheehan J P *et al* 2014 Temperature gradients due to adiabatic plasma expansion in a magnetic nozzle *Plasma Sources Sci. Technol.* **23** 045014
Sheppard A J and Little J M 2020 Scaling laws for electrodeless plasma propulsion with water vapor. propellant *Plasma Sources Sci. Technol.* **29** 045007
Singh N, Rao S and Ranganath P 2013 Waves generated in the plasma plume of helicon magnetic nozzle *Phys. Plasmas* **20** 032111
Stangeby P C, Canik J M and Whyte D G 2010 The relation between upstream density and temperature widths in the scrape-off layer and the power width in an attached divertor *Nucl. Fusion* **50** 125003
Sutton G P and Biblarz O 2016 *Rocket Propulsion Elements* (New York: Wiley)
Takahashi K *et al* 2011b Direct thrust measurement of a permanent magnet helicon double layer thruster *Appl. Phys. Lett.* **98** 141503
Takahashi K 2019 Helicon-type radiofrequency plasma thrusters and magnetic plasma nozzles *Rev. Mod. Plasma Phys.* **31** 1–61
Takahashi K, Akahoshi H, Charles C, Boswell R W and Ando A 2017a High temperature electrons exhausted from RF plasma sources along a magnetic nozzle *Phys. Plasmas* **24** 084503
Takahashi K and Ando A 2017b Laboratory observation of a plasma-flow-state transition from diverging to stretching a magnetic nozzle *Phys. Rev. Lett.* **118** 225002
Takahashi K, Charles C, Boswell R W and Ando A 2020a Thermodynamic analogy for electrons interacting with a magnetic nozzle *Phys. Rev. Lett.* **125** 165001
Takahashi K, Charles C, Boswell R W and Fujiwara T 2011a Electron energy distribution of a current-free. double layer: Druyvesteyn theory and experiments *Phys. Rev. Lett.* **107** 035002
Takahashi K, Charles C, Boswell R and Ando A 2018 Adiabatic expansion of electron gas in a magnetic nozzle *Phys. Rev. Lett.* **120** 045001
Takahashi K, Charles C, Boswell R, Cox W and Hatakeyama R 2009 Transport of energetic electrons in a magnetically expanding helicon double layer plasma *Appl. Phys. Lett.* **94** 191503
Takahashi K and Imai R 2022 Two-dimensional deflection of a plasma plume exhausted from a magnetically steered radiofrequency plasma thruster *Phys. Plasmas* **29** 054501
Takahashi K, Takao Y and Ando A 2020b Increased thrust-to-power ratio of a stepped-diameter helicon plasma thruster with krypton propellant *J. Propuls. Power* **36** 961–5
Versolato O 2019 Physics of laser-driven tin plasma sources of EUV radiation for nanolithography *Plasma Sources Sci. Technol.* **28** 083001
Vialis T, Jarrige J, Aanesland A and Packan D 2018 Direct thrust measurement of an electron cyclotron. Resonance plasma thruster *J. Propuls. Power* **34** 1323–33
Vinci A E, Delavière–Delion Q and Mazouffre S 2022 Electron thermodynamics along magnetic nozzle lines in a helicon plasma *J. Electric Propuls.* **1** 1–12
Winglee R, Ziemba T, Giersch L, Prager J, Carscadden J and Roberson B R 2007 Simulation and laboratory validation of magnetic nozzle effects for the high power helicon thruster *Phys. Plasmas* **14** 063501
Zawaideh E, Kim N S and Najmabadi F 1988 Generalized parallel heat transport equations in collisional to weakly collisional plasmas *Phys. Fluids* **31** 3280
Zhang Y, Charles C and Boswell R 2016a Thermodynamic study on plasma expansion along a divergent magnetic field *Phys. Rev. Lett.* **116** 025001
Zhang Y, Charles C and Boswell R 2016b A polytropic model for space and laboratory plasmas described by bi-Maxwellian electron distributions *Astrophys. J.* **829** 10
Zhou J, Domínguez-Vázquez A, Fajardo P and Ahedo E 2022 Magnetized fluid electron model within a two-dimensional hybrid simulation code for electrodeless plasma thrusters *Plasma Sources Sci. Technol.* **31** 045021
Zhou J, Sánchez-Arriaga G and Ahedo E 2021 Time-dependent expansion of a weakly-collisional plasma beam in a paraxial magnetic nozzle *Plasma Sources Sci. Technol.* **30** 045009
Ziemba T, Carscadden J, Slough J, Prager J and Winglee R 2005 High power helicon thruster *41st. AIAA/ASME/SAE/ASEE Joint Propulsion Conf. & Exhibit* p 4119